Article

Photophysical and Structural Properties of Cyanoruthenate Complexes of Hexaazatriphenylene

Juan-Manuel Herrera, Simon J. A. Pope, Anthony J. H. M. Meijer, Timothy L. Easun, Harry Adams, Wassim Z. Alsindi, Xue-Zhong Sun, Michael W. George, Stephen Faulkner, and Michael D. Ward

J. Am. Chem. Soc., **2007**, 129 (37), 11491-11504• DOI: 10.1021/ja072672w • Publication Date (Web): 22 August 2007

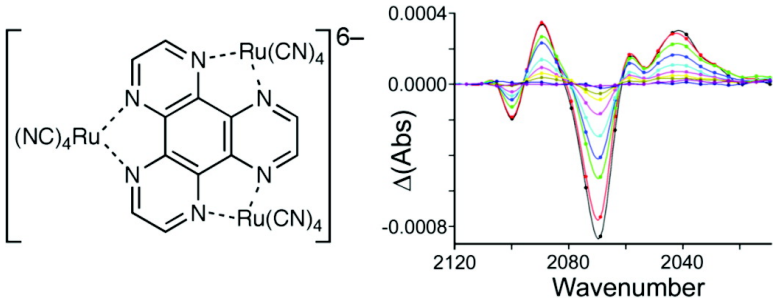

More About This Article

Additional resources and features associated with this article are available within the HTML version:

- Supporting Information
- Links to the 5 articles that cite this article, as of the time of this article download
- Access to high resolution figures
- Links to articles and content related to this article
- Copyright permission to reproduce figures and/or text from this article

View the Full Text HTML

J|A|C|S
ARTICLES
Published on Web 08/22/2007

Photophysical and Structural Properties of Cyanoruthenate Complexes of Hexaazatriphenylene

Juan-Manuel Herrera,[†] Simon J. A. Pope,[‡] Anthony J. H. M. Meijer,[†] Timothy L. Easun,[†] Harry Adams,[†] Wassim Z. Alsindi,[§] Xue-Zhong Sun,[§] Michael W. George,[§] Stephen Faulkner,[||] and Michael D. Ward*,[†]

Contribution from the Department of Chemistry, University of Sheffield, Sheffield S3 7HF, U.K., School of Chemistry, Main Building, Cardiff University, Cardiff CF10 3AT, U.K., School of Chemistry, University of Nottingham, University Park, Nottingham NG7 2RD, U.K., and Department of Cmemistry, University of Manchester, Oxford Road, Manchester M13 9PL, U.K.

Received April 30, 2007; Revised Manuscript Received July 4, 2007; E-mail: m.d.ward@sheffield.ac.uk

Abstract: The tritopic bridging ligand hexaazatriphenylene (HAT) has been used to prepare the mono-, di-, and trinuclear cyanoruthenate complexes $[Ru(CN)_4(HAT)]^{2-}$ ($[\mathbf{1}]^{2-}$), $[\{Ru(CN)_4\}_2(\mu_2\text{-HAT})]^{4-}$ ($[\mathbf{2}]^{4-}$), and $[\{Ru(CN)_4\}_3(\mu_3\text{-HAT})]^{6-}$ ($[\mathbf{3}]^{6-}$). These complexes are of interest both for their photophysical properties and ability to act as sensitizers, associated with strong MLCT absorptions; and their structural properties, with up to 12 externally directed cyanide ligands at a single "node" for preparation of coordination networks. The complexes are strongly solvatochromic, with broad and intense MLCT absorption manifolds arising from the presence of low-lying π^* orbitals on the HAT ligand, as confirmed by DFT calculations; in aprotic solvents $[\mathbf{3}]^{6-}$ is a panchromatic absorber of visible light. Although nonluminescent in fluid solution, the lowest MLCT excited states have lifetimes in D_2O of tens of nanoseconds and could be detected by time-resolved IR spectrosocopy. For dinuclear $[\mathbf{2}]^{4-}$ and trinuclear $[\mathbf{3}]^{6-}$ the TRIR spectra are indicative of asymmetric MLCT excited states containing distinct Ru(III) and Ru(II) centers on the IR time scale. The complexes show red ^{3}MLCT luminescence as solids and in EtOH/MeOH glass at 77 K. Ln(III) salts of $[\mathbf{1}]^{2-}$, $[\mathbf{2}]^{4-}$, and $[\mathbf{3}]^{6-}$ form infinite coordination networks based on Ru−CN−Ln bridges with a range of one-, two-, and three-dimensional polymeric structures. In the Yb(III) and Nd(III) salts of $[\mathbf{3}]^{6-}$ the complex anion forms an 8-connected node. Whereas all of the Gd(III) salts show strong ^{3}MLCT luminescence in the solid state, the Ru-based emission in the Nd(III) and Yb(III) analogues is substantially quenched by Ru → Ln photoinduced energy transfer, which results in sensitized near-infrared luminescence from Yb(III) and Nd(III).

Introduction

The complex $[Ru(bipy)(CN)_4]^2$, first reported by Bignozzi and Scandola in 1986, has a particularly attractive set of properties which make it of interest in the general area of syntheses and photophysical properties of supramolecular assemblies.[1−3] Like its better-known cousin $[Ru(bipy)_3]^{2+}$ it has a luminescent Ru → bipy ^{3}MLCT excited state, which is relatively long-lived (≈100 ns) in protic solvents. In addition to this moreover it has several other advantages from both a synthetic and a spectroscopic viewpoint. From the structural point of view, it is exceptionally easy to incorporate into supramolecular assemblies because the cyanide groups can participate in either coordination to additional metal ions[4−6] or in hydrogen-bonding with molecules containing acidic protons,[7−10] and both of these mechanisms have been used to prepare noncovalently linked assemblies in which $[Ru(bipy)(CN)_4]^{2-}$ acts as an energy donor or acceptor in its excited state.[2] In particular we have prepared cyanide-bridged coordination networks combining $[Ru(bipy)(CN)_4]^{2-}$ as a visible light-absorbing sensitizer unit with lanthanide(III) ions such as Nd(III), Er(III), Pr(III), and Yb(III) as energy-acceptors, allowing generation of sensitized near-infrared luminescence from these

[†] University of Sheffield.
[‡] University of Cardiff.
[§] University of Nottingham.
[||] University of Manchester.

(1) (a) Bignozzi, C. A.; Chiorboli, C.; Indelli, M. T.; Scandola, M. A. R.; Varani, G.; Scandola, F. *J. Am. Chem. Soc.* **1986**, *108*, 7872. (b) Habib Jiwan, J. L.; Wegewijs, B.; Indelli, M. T.; Scandola, F.; Braslavsky, S. E. *Recl. Trav. Chim. Pays-Bas* **1995**, *114*, 542.
(2) Ward, M. D. *Coord. Chem. Rev.* **2006**, *250*, 3128.
(3) Timpson, C. J.; Bignozzi, C. A.; Sullivan, B. P.; Kober, E. M.; Meyer, T. J. *J. Phys. Chem.* **1996**, *100*, 2915.
(4) (a) Davies, G. M.; Pope, S. J. A.; Adams, H.; Faulkner, S.; Ward, M. D. *Inorg. Chem.* **2005**, *44*, 4656. (b) Miller, T. A.; Jeffery, J. C.; Ward, M. D.; Adams, H.; Pope, S. J. A.; Faulkner, S. *Dalton Trans.* **2004**, 1524. (c) Baca, S. G.; Adams, H.; Ward, M. D. *Cryst. Eng. Commun.* **2006**, *88*, 635.
(5) (a) Herrera, J.-M.; Pope, S. J. A.; Adams, H.; Faulkner, S.; Ward, M. D. *Inorg. Chem.* **2006**, *45*, 3895. (b) Herrera, J.-M.; Baca, S.; Ward, M. D. *Polyhedron* **2006**, *25*, 869.
(6) Lazarides, T.; Easun, T. L.; Veyne-Marti, C.; Alsindi, W. Z.; George, M. W.; Deppermann, N.; Hunter, C. A.; Adams, H.; Ward, M. D. *J. Am. Chem. Soc.* **2007**, *129*, 4014.
(7) Derossi, S.; Adams, H.; Ward, M. D. *Dalton Trans.* **2007**, 33.
(8) Simpson, N. R. M.; Ward, M. D.; Morales, A. F.; Ventura, B.; Barigelletti, F. *J. Chem. Soc., Dalton Trans.* **2002**, 2455.
(9) Pina, F.; Parola, A. J. *Coord. Chem. Rev.* **1999**, *185−186*, 149.
(10) Bergamini, G.; Saudan, C.; Ceroni, P.; Maestri, M.; Balzani, V.; Gorka, M.; Lee, S.-K.; van Heyst, J.; Vögtle, F. *J. Am. Chem. Soc.* **2004**, *126*, 16466.

Ln(III) centers following d → f energy-transfer.[4] From the spectroscopic point of view, $[Ru(bipy)(CN)_4]^{2-}$ is strongly solvatochromic, with its ^{1}MLCT and ^{3}MLCT levels and Ru(II)/Ru(III) redox potential varying over a wide range in different solvents due to different degrees of hydrogen-bonding between the cyanide lone pairs and the solvent: the ^{3}MLCT emission maximum varies from 610 nm in water to ≈800 nm in non H-bonding solvents such as MeCN and dmf.[1−3] Interaction of the cyanide ligands with additional metal cations in solution has an even stronger effect, with "metallochromism" allowing the ^{3}MLCT energy to be varied over a range of ca. 6000 cm^{-1}.[6] Thus, the ability of $[Ru(bipy)(CN)_4]^{2-}$ to act as an energy donor in its excited state can be tuned by varying the solvent composition or by addition of group 1A or 2A metal salts to the solvent, which has been exploited as the basis of interesting switching effects such as reversal of the direction of energy transfer in a dyad.[6,11] Finally, the cyanide group provides a convenient spectroscopic handle for monitoring the excited state using transient infrared spectroscopy since the position of the CN vibrations is sensitive to the electron distribution in the complex.[12,13]

Higher nuclearity analogues of $[Ru(bipy)(CN)_4]^{2-}$ have been scarcely studied and have considerable appeal because many of the above advantages will be amplified. A larger number of cyanide groups present in a single molecule will allow preparation of structurally novel luminescent materials with a higher degree of connectivity to a single node, and should also allow for a greater degree of modulation of the spectroscopic properties via solvatochromism and metallochromism effects, since these depend on the number of cyanide sites available.[3] We recently prepared dinuclear $[\{Ru(CN)_4\}_2(\mu\text{-bpym})]^{4-}$ (bpym = 2,2′-bipyrimidine) and used it as the basis of coordination networks with lanthanide cations.[5] Up to six of the eight cyanide groups were found to be involved in bridging interactions to Ln(III) centers, and picosecond time-resolved IR studies showed that it has an asymmetric, valence-trapped ^{3}MLCT excited state $[(NC)_4Ru^{II}(bpym^{\bullet-})Ru^{III}(CN)_4]^{4-}$.[13]

In this paper, we describe the syntheses, spectroscopic, and some structural properties of the series of complexes $[Ru(CN)_4(HAT)]^{2-}$ ($[\mathbf{1}]^{2-}$), $[\{Ru(CN)_4\}_2(\mu_2\text{-HAT})]^{4-}$ ($[\mathbf{2}]^{4-}$), and $[\{Ru(CN)_4\}_3(\mu_3\text{-HAT})]^{6-}$ ($[\mathbf{3}]^{6-}$) (Scheme 1) in which one, two, or three $\{Ru(CN)_4\}^{2-}$ units are connected to the bidentate sites of the tritopic ligand hexaazatriphenylene (HAT).[14] These complexes prove to have some very interesting properties. The low energy of the LUMO of the extended aromatic bridging ligand and the presence of up to three Ru(II) centers means that the ^{1}MLCT absorptions are low energy and intense; there are obvious parallels with Ru(II) and Os(II) complexes of other highly extended aromatic diimine-based ligands such as eilatin/dibenzoeilatin[15] and the "heterosuperbenzenes"[16] which show

Scheme 1

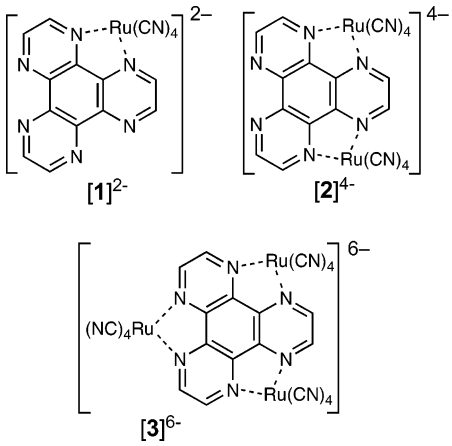

unusually low energy absorption and emission bands. The presence of up to 12 cyanide groups which can interact with solvent molecules is expected to provide a high degree of solvatochromism. In addition the potential connectivity of up to 12 provided by the externally directed cyanide binding sites of $[\{Ru(CN)_4\}_3(\mu_3\text{-HAT})]^{6-}$ is unprecedented in cyanide-based coordination networks. The highest connectivity observed so far at a single cyanometalate node is eight, in a network in which all eight cyanides of $[W(CN)_8]^{4-}$ are coordinated to Co(II) ions,[17] although this is rare: usually octacyanometalates of Mo and W connect to six or less other metal cations.[18] Accordingly this series of high-nuclearity cyanoruthenates, with up to 12 externally directed cyanide ligands, is expected to be of interest equally for its structural properties and its photophysical properties, and we describe here an extensive investigation into both aspects of the chemistry of $[\mathbf{1}]^{2-}$, $[\mathbf{2}]^{4-}$, and $[\mathbf{3}]^{6-}$. A preliminary Communication describing a small part of this work has been published recently.[19]

Results and Discussion

Synthesis and Characterization. Reaction of the tritopic ligand HAT with 3.6 equiv of $K_4[Ru(CN)_6]\cdot 3H_2O$ in aqueous acid (pH 1.3) at reflux for 48 h afforded a deep violet solution from which the complexes $[\mathbf{1}]^{2-}$ (orange-red), $[\mathbf{2}]^{4-}$ (deep red), and $[\mathbf{3}]^{6-}$ (violet) could be isolated as their sodium salts by ion-exchange chromatography on Sephadex QAE-25 eluting with aqueous NaI. In this form the complexes are isolated as their sodium salts and are water-soluble; to render them soluble in organic solvents, the complexes were converted to their PPN^+ salts (PPN^+ is $Ph_3P{=}N{=}PPh_3^+$), which are soluble in polar organic solvents such as MeCN and dmf.[20] The complexes were satisfactorily characterized on the basis of elemental analyses, negative-ion electrospray mass spectra, and ^{1}H NMR spectra.

(11) (a) Simpson, N. R. M.; Ward, M. D.; Morales, A. F.; Barigelletti, F. *J. Chem. Soc., Dalton Trans.* **2002**, 2449. (b) Indelli, M. T.; Ghirotti, M.; Prodi, A.; Chiorboli, C.; Scandola, F.; McClenaghan, N. D.; Puntoriero, F.; Campagna, S. *Inorg. Chem.* **2003**, *42*, 5489.
(12) Adams, H.; Alsindi, W.; Davies, G. M.; Duriska, M. B.; Easun, T. L.; Fenton, H.; Herrera, J.-M.; George, M. W.; Ronayne, K. L.; Sun, X.-Z.; Towrie, M.; Ward, M. D. *Dalton Trans.* **2006**, 39.
(13) Alsindi, W. Z.; Easun, T. L.; Sun, X.-Z.; Ronayne, K. L.; Towrie, M.; Herrera, J.-M.; George, M. W.; Ward, M. D. *Inorg. Chem.* **2007**, *46*, 3696.
(14) (a) Kitagawa, S.; Masaoka, S. *Coord. Chem. Rev.* **2003**, *246*, 73. (b) Patra, S.; Sarkar, B.; Ghumaan, S.; Fiedler, J.; Kaim, W.; Lahiri, G. K. *Dalton Trans.* **2004**, 754. (c) D'Alessandro, D.; Keene, F. R. *Chem.—Eur. J.* **2005**, *11*, 3679. (d) Leveque, J.; Moucheron, C.; Kirsch-De Mesmaeker, A.; Loiseau, F.; Serroni, S.; Puntoriero, F.; Campagna, S.; Nierengarten, H.; van Dorsselaer, A. *Chem. Commun.* **2004**, 878.
(15) (a) Bergman, S. D.; Gut, D.; Kol, M.; Sabatini, C.; Barbieri, A.; Barigelletti, F. *Inorg. Chem.* **2005**, *44*, 7943. (b) Bergman, S. D.; Goldberg, I.; Barbieri, A.; Kol, M. *Inorg. Chem.* **2005**, *44*, 2513.
(16) (a) Draper, S. M.; Gregg, D. J.; Schofield, E. R.; Browne, W. R.; Duati, M.; Vos, J. G.; Passaniti, P. *J. Am. Chem. Soc.* **2004**, *126*, 8694. (b) Gregg, D. J.; Bothe, E.; Hofer, P.; Passaniti, P.; Draper, S. M. *Inorg. Chem.* **2005**, *44*, 5654. (c) Gregg, D. J.; Fitchett, C. M.; Draper, S. M. *Chem. Commun.* **2006**, 3090.
(17) Herrera, J.-M.; Bleuzen, A.; Dromzée, Y.; Julve, M.; Lloret, F.; Verdaguer, M. *Inorg. Chem.* **2003**, *42*, 7052.
(18) Sieklucka, B.; Podgajny, R.; Przychodzen, P.; Korzeniak, T. *Coord. Chem. Rev.* **2005**, *249*, 2203.
(19) Herrera, J.-M.; Ward, M. D.; Adams, H.; Pope, S. J. A.; Faulkner, S. *Chem. Commun.* **2006**, 1851.
(20) Evju, J. K.; Mann, K. R. *Chem. Mater.* **1999**, *11*, 1425.

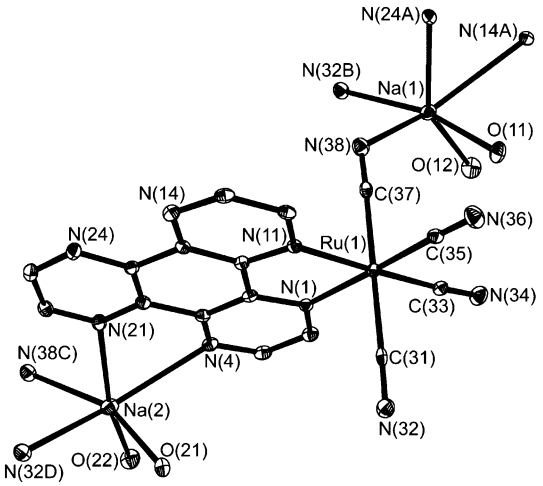

Figure 1. Asymmetric unit of the structure of $Na_2[\mathbf{1}]\cdot 4H_2O$, with additional atoms from adjacent asymmetric units to complete the coordination spheres around Na(1) and Na(2) included.

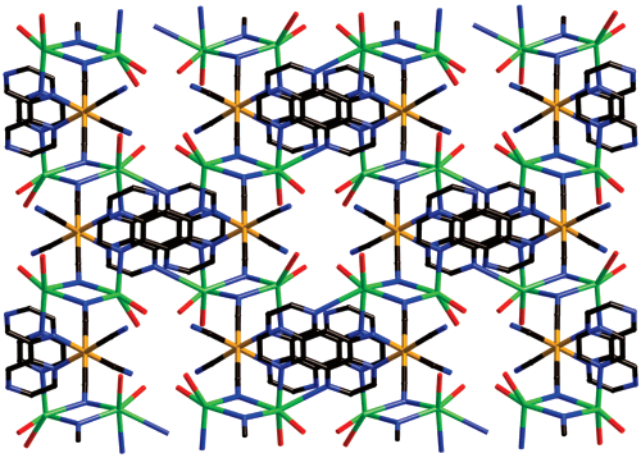

Figure 2. Network structure of $Na_2[\mathbf{1}]\cdot 4H_2O$ (Na, green; Ru, orange; O, red; N, blue; C, black).

In particular, the ^{1}H NMR spectra for $[\mathbf{1}]^{2-}$ and $[\mathbf{2}]^{4-}$ show three signals (two doublets and a singlet) for the HAT ligand, as expected for C_{2v} symmetry; for the more highly symmetric complex $[\mathbf{3}]^{6-}$ a single resonance is seen for the HAT ligand.

Slow evaporation of an aqueous solution of $Na_2[\mathbf{1}]$ afforded X-ray-quality crystals of $Na_2[\mathbf{1}]\cdot 4H_2O$ whose structure is shown in Figures 1 and 2 (see also Table 1). The structure of the $[Ru(HAT)(CN)_4]^{2-}$ anionic fragment is unremarkable, with octahedral coordination around the Ru(II) center and essentially linear cyanide ligands (Ru−C−N angles between 177 and 178°). Coordination of both cyanide groups and diimine sites of the HAT ligand to the Na^+ counterions results in formation of a coordination network. Na(1) and Na(2) are both six-coordinate, from two water ligands, two cyanides (from two different $[\mathbf{1}]^{2-}$ units), and a diimine site from a third $[\mathbf{1}]^{2-}$ unit. Thus, all three bidentate sites of the HAT ligand are occupied, one by the $\{Ru(CN)_4\}^{2-}$ unit and the other two by Na^+ cations, although the interaction between the bidentate HAT sites and each Na^+ ion is markedly asymmetric, with one short Na−N bond [Na(1)−N(24), 2.43 Å; Na(2)−N(21), 2.46 Å] and one long bond [Na(1)−N(14), 2.97 Å; Na(2)−N(4), 2.88 Å]. Na(1) and Na(2) are close together (3.91 Å) and bridged by the two cyanide ligands N(32) and N(38), which are the axial pair from $[\mathbf{1}]^{2-}$. The equatorial pair of cyanide ligands [containing N(34) and N(36)] are not involved in coordination to Na^+ ions but are involved in OH···NC hydrogen-bonding to water ligands on the Na^+ ions, with two nonbonded O···N separations of <3Å for each of these N atoms. The network as a whole is shown in Figure 2.

Table 1. Selected Bond Distances in the Structure of $Na_2[\mathbf{1}]\cdot 4H_2O$[a]

Ru(1)−C(35)	1.981(9)	Na(1)−N(38)	2.600(9)
Ru(1)−C(33)	1.988(9)	Na(1)−N(14)$^{\#3}$	2.967(8)
Ru(1)−C(37)	2.043(9)	Na(1)−Na(2)$^{\#1}$	3.907(6)
Ru(1)−C(31)	2.051(9)	Na(2)−O(22)	2.295(8)
Ru(1)−N(11)	2.101(7)	Na(2)−O(21)	2.336(8)
Ru(1)−N(1)	2.112(7)	Na(2)−N(21)	2.459(8)
Na(1)−O(12)	2.343(8)	Na(2)−N(38)$^{\#1}$	2.514(9)
Na(1)−O(11)	2.347(8)	Na(2)−N(32)$^{\#2}$	2.691(9)
Na(1)−N(24)$^{\#3}$	2.431(8)	Na(2)−N(4)	2.881(9)
Na(1)−N(32)$^{\#4}$	2.465(9)	Na(2)−Na(1)$^{\#1}$	3.907(6)
Na(1)−N(38)	2.600(9)		

[a] Symmetry transformations used to generate equivalent atoms: (#1) $-x+1, -y, -z+1$; (#2) $-x+1/2, y-1/2, -z+3/2$; (#3) $-x+1/2, y+1/2, -z+1/2$; (#4) $x+1/2, -y+1/2, z-1/2$.

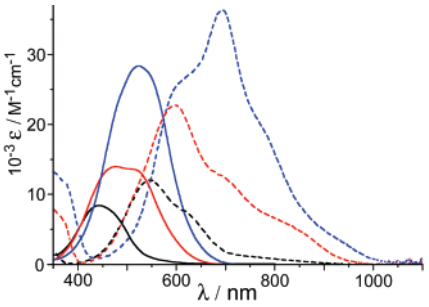

Figure 3. Electronic absorption spectra of $[\mathbf{1}]^{2-}$ (black), $[\mathbf{2}]^{4-}$ (red), and $[\mathbf{3}]^{6-}$ (blue), in water (solid lines) and dmf (dashed lines).

UV/Vis Spectroscopic Properties. The intense colors of these complexes arise from ^{1}MLCT absorptions,[1−3] which are lower in energy than those of the parent complex $[Ru(bipy)(CN)_4]^{2-}$ because the extended aromatic framework of the HAT ligand means that its π^* orbitals are relatively low in energy. For mononuclear $[\mathbf{1}]^{2-}$ the absorption maximum in aqueous solution is at 443 nm; cf. 400 nm for $[Ru(bipy)(CN)_4]^{2-}$. Coordination of the second and third metal centers to give $[\mathbf{2}]^{4-}$ and $[\mathbf{3}]^{6-}$ results in (i) a red-shift of this absorption maximum to 478 and then 524 nm, respectively, in water and (ii) an approximate trebling in the extinction coefficient to 28 000 M^{-1} cm^{-1} in $[\mathbf{3}]^{6-}$ (Figure 3).

The solvatochromism of complexes of this type is well-known and is related to the number of cyanide ligands available for interaction with the solvent.[2] Thus, for example, $[Ru(bipy)(CN)_4]^{2-}$ with four cyanides shows a greater variation in its absorption and emission energies than $[Ru(bipy)_2(CN)_2]$ which has only two cyanides. Accordingly we expect that the solvatochromic behavior of these complexes should become more pronounced ($[\mathbf{1}]^{2-} < [\mathbf{2}]^{4-} < [\mathbf{3}]^{6-}$) as the number of cyanide ligands goes from 4 to 8 to 12. The data in five different solvents are summarized in Table 2; see also Figure 3 for extreme cases of the spectra, in water and dmf.

For complex $[\mathbf{1}]^{2-}$ the lowest energy ^{1}MLCT absorption maximum occurs at 443 nm (water), 482 nm (MeOH), 523 nm (CH_2Cl_2), 527 nm (MeCN), and 546 nm (DMF), showing a shift to lower energy as the solvent becomes a poorer hydrogen-bond donor; there is an obvious correlation with the Gutmann acceptor number of the solvent, a parameter which provides a

Table 2. Absorption Maxima Associated with ^{1}MLCT Transitions of the Complexes in Different Solvents

	λ_{max}/nm ($10^{-3}\epsilon$, M^{-1} cm^{-1})				
compd	H_2O[a]	CH_3OH[a]	CH_3CN[b]	CH_2Cl_2[b]	DMF[b]
$[\mathbf{1}]^{2-}$	443 (8.2)	482 (8.8)	527 (12)	523 (11)	546 (11)
			578 (sh)	579 (sh, ≈8)	618 (sh, ≈7)
$[\mathbf{2}]^{4-}$	478 (14)	520 (16)	576 (21)	572 (22)	596 (23)
			657 (sh, ≈14)	644 (sh, ≈14)	692 (13)
	516 (sh)	571 (sh)	780 (sh, ≈6)	744 (sh, ≈6)	805 (6.4)
$[\mathbf{3}]^{6-}$	524 (28)	575 (28)	602 (sh, ≈27)	593 (sh, ≈26)	610 (sh, ≈26)
			666 (35)	632 (33)	692 (36)
			739 (sh, ≈21)	705 (sh, 21)	762 (sh, ≈21)

[a] Na^+ salt used for solubility in more polar solvents. [b] $(PPN)^+$ salt used for solubility in less polar solvents.

measure of the Lewis acidity of a particular solvent.[21] The shift in the energy of the absorption maximum between the extremes of water and dmf is 4260 cm^{-1}, which is significantly less than observed for $[Ru(bipy)(CN)_4]^{2-}$ [$\Delta(\lambda_{max}) = 6860$ cm^{-1} between the same two solvents].[3] This implies that the interaction between the cyanide lone pairs and the Lewis acidic solvents is weaker in $[\mathbf{1}]^{2-}$ than in $[Ru(bipy)(CN)_4]^{2-}$, a reasonable conclusion given the stronger π-accepting nature of HAT compared to bipy which will remove more electron density from the Ru(II) center of $[\mathbf{1}]^{2-}$ and make the cyanide lone pairs weaker donors compared to $[Ru(bipy)(CN)_4]^{2-}$. However, we note that in dmf the ^{1}MLCT absorption maximum has a more complicated profile than it does in water, with a pronounced low-energy shoulder at 620 nm and a weaker one between 700 and 750 nm which extends the tail of the absorption spectrum out to >900 nm. There are therefore several closely spaced ^{1}MLCT components which are not resolved in water and give an apparently single absorption band, but these spread out in solvents with a lower Gutmann acceptor number (see below for a computational analysis).

For dinuclear $[\mathbf{2}]^{4-}$ the presence of at least two components to the ^{1}MLCT absorption manifold is obvious even in water, where the spectrum displays a maximum at 478 nm and a shoulder of nearly the same intensity at 516 nm; in dmf the most intense peak is red-shifted to 596 nm, but there are two intense lower energy shoulders at ≈700 and 825 nm which result in the absorption spectrum extending out to ≈1000 nm. The red-shift in the most intense absorption component between water and dmf is 4140 cm^{-1}, which is actually less than for $[\mathbf{1}]^{2-}$ despite the larger number of cyanide ligands, but this obviously does not tell the whole story as the lower energy absorption components are much more strongly red-shifted (ca. 7200 cm^{-1} for the lowest energy feature). The same general behavior occurs for $[\mathbf{3}]^{6-}$. The main ^{1}MLCT absorption band in water is at 524 nm and is rather broad, indicative of two or more closely spaced components; in dmf these have spread out to the extent that four components are clearly visible, with the lowest energy feature—a shoulder at ca. 930 nm—extending the low-energy tail out to ca. 1050 nm. The red-shift in the absorption maximum between water and dmf is 4630 cm^{-1}, comparable to that seen for $[\mathbf{1}]^{2-}$ and $[\mathbf{2}]^{4-}$, but again it is the lower energy features that are far more dramatically red-shifted to the extent of >8000 cm^{-1} for the lowest energy feature in the spectrum of $[\mathbf{3}]^{6-}$. This results in panchromatic absorbance of light all the way across the visible region and extending well into the near-infrared. This is a particularly desirable characteristic for complexes used in dye-sensitized solar cells as it results in effective photocurrent generation throughout the solar emission spectrum, and considerable synthetic effort has gone into the design and synthesis of complexes which display panchromatic absorption in this way.[22] Indeed, in dmf complexes $[\mathbf{2}]^{4-}$ and $[\mathbf{3}]^{6-}$ have light-absorbing characteristics superior to those of the $[Ru(terpy)(NCS)_3]^-$ derivatives used as "black" dyes in solar cells, with much higher extinction coefficients and a longer low-energy absorption tail.[22c,e]

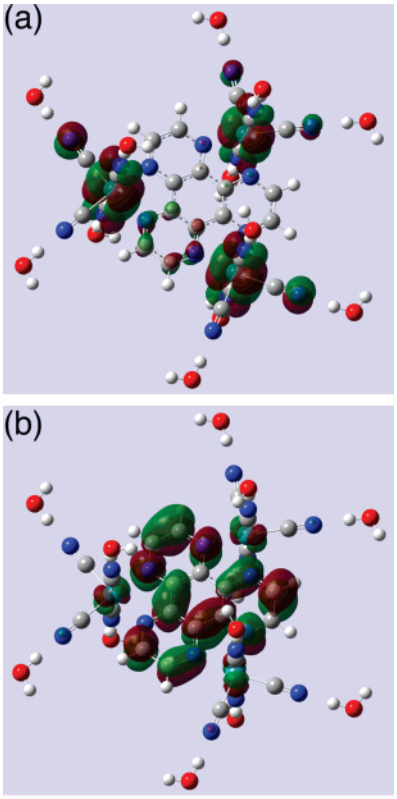

Figure 4. HOMO and LUMO of the hydrated cluster $[\mathbf{3}]^{6-}\cdot 12H_2O$ calculated using DFT methods (see main text).

Molecular Orbital Calculations. DFT calculations using GAUSSIAN were performed on $[\mathbf{3}]^{6-}$ to determine the nature of the frontier orbitals and rationalize the electronic spectra. The HOMO and LUMO calculated in the presence of specific hydrogen-bonding interactions to water (modeled by one CN···HOH interaction/cyanide, with an N···O separation after geometry optimization of 2.7 Å) are shown in Figure 4. The HOMO is largely based on the Ru d(π) orbital set (with a small contribution from the cyanides), and the LUMO is localized on the HAT ligand. Thus, the lowest-energy electronic transition can be assigned with confidence as ^{1}MLCT. What differentiates this complex from simple mononuclear species such as $[Ru(bipy)(CN)_4]^-$ is the presence of a manifold of six closely spaced π^* orbitals on the HAT ligand and likewise six closely

(21) Gutmann, V.; Resch, G.; Linert, W. *Coord. Chem. Rev.* **1982**, *43*, 133.

(22) (a) Yanagida, M.; Yamaguchi, T.; Kurashige, M.; Hara, K.; Katoh, R.; Sugihara, H.; Arakawa, H. *Inorg. Chem.* **2003**, *42*, 7921. (b) Islam, A.; Sugihara, H.; Yanagida, M.; Hara, K.; Fujihashi, G.; Tachibana, Y.; Katoh, R.; Murata, S.; Arakawa, H. *New J. Chem.* **2002**, *26*, 966. (c) Nazeeruddin, M. K.; Pechy, P.; Renouard, T.; Zakeeruddin, S. M.; Humphry-Baker, R.; Comte, P.; Liska, P.; Cevey, L.; Costa, E.; Shklover, V.; Spiccia, L.; Deacon, G. B.; Bignozzi, C. A.; Grätzel, M. *J. Am. Chem. Soc.* **2001**, *123*, 1613. (d) Grätzel, M. *Inorg. Chem.* **2005**, *44*, 6841. (e) Ghosh, S.; Chaitanya, G. K.; Bhanuprakash, K.; Nazeeruddin, M. K.; Grätzel, M.; Reddy, P. Y. *Inorg. Chem.* **2006**, *45*, 7600.

spaced occupied orbitals of principally Ru-centered 4d character. Thus, a large collection of closely spaced ^{1}MLCT absorptions is expected, as we observe.

To investigate this further we calculated the excitation energies for $[\mathbf{1}]^{2-}$, $[\mathbf{2}]^{4-}$, and $[\mathbf{3}]^{6-}$ in DMF and in H_2O using the TD−DFT method. TD−DFT has well-publicized problems with MLCT states, and therefore, we cannot expect a quantitatively correct answer.[23] However, because the errors for each compound will be similar, we *can* use these results to get a qualitative understanding of the photophysics.

The lowest 10 excitation energies for each compound are given in Table S1 (Supporting Information); the coordinates for the calculated energy-minimized structures used in the calculations are in Table S2. It is clear from the calculations that the excitation energies for the compounds dissolved in DMF are generally lower than for the same compounds dissolved in water, in agreement with the experimental data. It is also apparent that the calculated excitation energies decrease with increasing number of Ru atoms in the complex, again in agreement with experimental data (see Table 2). Thus, for the series $[\mathbf{1}]^{2-}$, $[\mathbf{2}]^{4-}$, and $[\mathbf{3}]^{6-}$, the lowest energy absorptions are calculated as 738, 761, and 792 nm, respectively, in dmf and 664, 700, and 741 nm, respectively, in water. Note that, due to the fact that no symmetry was imposed on the calculations, expected degeneracies in the excitation energies will be slightly lifted due to numerical rounding errors.

The effect of changing solvent from water to dmf in these calculations is not as large as we observed experimentally. For example, the lowest 10 MLCT excitations for $[\mathbf{3}]^{6-}$ are calculated by this method to lie in the range 701−792 nm in dmf and between 663 and 741 nm in water, giving an average blue-shift of ca. 850 cm^{-1} in water, much less than actually observed (see previous section). This is probably partially due to the problems with using TD−DFT for charge-transfer states as indicated above; in addition our allowance of one hydrogen-bonded water molecule/cyanide ligand may be too modest, with much more extensive aquation being present in reality[24] which would result in a bigger difference between absorption energies in water and DMF. We note also that although DFT gives good geometries (even for van der Waals bonded systems), it generally significantly underestimates the van der Waals binding energy and will therefore underestimate the influence of the weakly bound water molecules on the electronic wave function of the complex.

To conclude this section, we emphasize that quantitative conclusions about the electronic spectra are not appropriate given the known difficulties in calculations of charge-transfer transitions using TD−DFT.[23] However the calculations do confirm that (i) a manifold of several closely spaced ^{1}MLCT absorptions is expected due to the presence of several low-lying π^* orbitals on the HAT ligand, (ii) the absorption manifold should be red-shifted as the number of metal centers increases, with $[\mathbf{3}]^{6-}$ having the lowest energy MLCT absorptions, and (iii) these MLCT absorptions should be red-shifted in the absence of hydrogen-bonding interactions, also as observed.

(23) (a) Dreeuw, A.; Head-Gordon, M. *Chem. Rev.* **2005**, *105*, 4009. (b) Dreeuw, A.; Weisman, J.; Head-Gordon, M. *J Chem. Phys.* **2003**, *119*, 2943. (c) Tozer, D. *J. Chem. Phys*. **2003**, *119*, 12697. (d) Tozer, D. J.; Amos, R. D.; Handy, N. C.; Roos, B. O.; Serrano-Andrés, L. *Mol. Phys*. **1999**, *97*, 859 and references therein.

(24) Megyes, T.; Schubert, G.; Kovács, M.; Radnai, T.; Grósz, T.; Bakó, I.; Pápai, I.; Horváth, A. *J. Phys. Chem. A* **2003**, *107*, 9903.

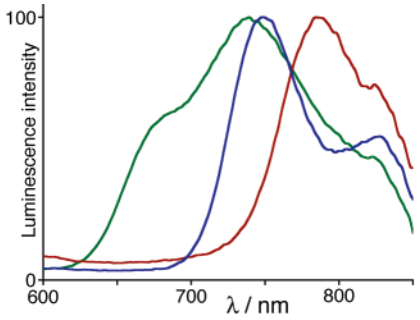

Figure 5. Normalized luminescence spectra (corrected for detector sensitivity) of $[\mathbf{1}]^{2-}$ (green), $[\mathbf{2}]^{4-}$ (blue), and $[\mathbf{3}]^{6-}$ (red), as their Na^+ salts in EtOH/MeOH (4:1, v/v) glass at 77 K.

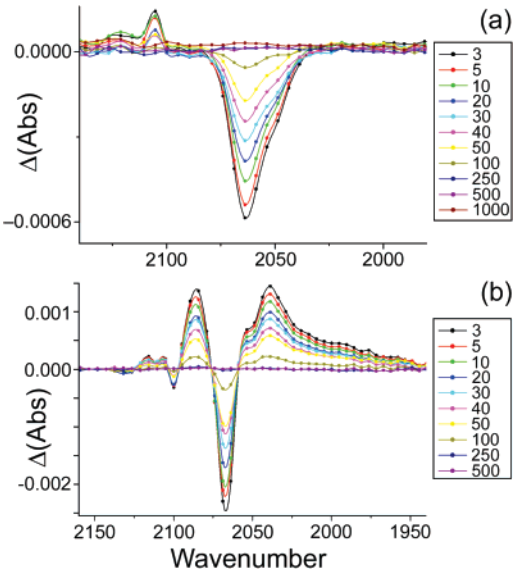

Figure 6. Time-resolved IR difference spectra of $[\mathbf{1}]^{2-}$ (top) and $[\mathbf{2}]^{4-}$ (bottom) in D_2O each measured at several time intervals after excitation. The key shows the time delay after excitation (in nanoseconds) at which each spectrum was recorded.

Excited-State Properties in Solution. No luminescence could be detected from these complexes in aqueous solution. Given the general pattern for $[Ru(bipy)(CN)_4]^{2-}$ derivatives that in less Lewis-acidic solvents the ^{3}MLCT energy is reduced in energy compared to water and the luminescence is weaker and shorter-lived,[1−3] we did not expect (and did not observe) luminescence in any other solvents either at room temperature. However in a 4:1 EtOH/MeOH glass at 77 K, weak luminescence bands were observed in each case with maxima (corrected for the detector response) at 739, 748, and 770 nm for $Na_2[\mathbf{1}]$, Na_4 [**2**], and $Na_6[\mathbf{3}]$, respectively (Figure 5), which gives ^{3}MLCT energies of 13 500, 13 400, and 13 000 cm^{-1}, respectively, under these conditions.

We examined the excited-state behavior of the complexes in solution by time-resolved infrared spectroscopy, which allows non- or poorly luminescent excited states to be observed by changes in their IR absorption spectra. Figure 6a shows the transient IR difference spectra in the ν(CN) region of $Na_2[\mathbf{1}]$ in D_2O with different time delays between pump and probe. The results are in agreement with what we have observed for other mononuclear complexes of the $[Ru(diimine)(CN)_4]^{2-}$ type.[12,13,25]

(25) Encinas, S.; Morales, A. F.; Barigelletti, F.; Barthram, A. M.; White, C. M.; Couchman, S. M.; Jeffery, J. C.; Ward, M. D.; Grills, D. C.; George, M. W. *J. Chem. Soc., Dalton Trans.* **2001**, 3312.

The strongest ground-state ν(CN) band at ca. 2066 cm^{-1} is bleached, and a weak transient band to higher energy (ca. 2110 cm^{-1}) is formed, both returning to the baseline on the same time scale with a lifetime of 44 ns. The transient band corresponds to the ν(CN) vibration in the excited state and is at higher energy because the MLCT process results in transient oxidation of the metal center from Ru(II) to Ru(III), which diminishes the Ru[d(π)] → CN(π^*) back-bonding and results in the C−N bond being strengthened. The shift of this band to higher energy by ca. 40 cm^{-1} is typical.[12,13,25] The transient band to higher energy is weak, for two reasons: (i) It overlaps with the bleach of the weak highest energy ν(CN) band at ca. 2100 cm^{-1}. (ii) The transient oxidation of the Ru center will diminish the dipole of the C−N bond, which is in the sense $C^{\delta-}-N^{\delta+}$, reducing the oscillator strength for the vibrational transition.

The TRIR difference spectra of the dinuclear complex Na_4-[**2**] in D_2O at different time delays are shown in Figure 6b. Interpretation of these spectra is aided by comparison with the homodinuclear complex $[\{Ru(CN)_4\}_2(\mu\text{-bpym})]^{4-}$ in which the ^{3}MLCT excited state was best described as having a valence-localized electronic structure $[(NC)_4Ru^{II}(bpym^{\bullet-})Ru^{III}(CN)_4]^{4-}$ on the IR time scale:[13] two sets of ν(CN) transient bands were apparent, one at higher energy corresponding to the transiently oxidized Ru(III) center and one at lower energy corresponding to the "spectating" Ru(II) center which was made more electron-rich by having electron density pushed toward it. The TRIR difference spectra of $[\mathbf{2}]^{4-}$ display a similar set of features. The main ground-state ν(CN) band at 2070 cm^{-1} is bleached, and two new transient bands are present, a weak one to higher energy and an intense one to lower energy. These all decay synchronously with a time constant of 56 ns. The high-energy transient is again weak and can be seen as a small positive-going feature at 2115 cm^{-1} [again, partially obscured by the bleach of the highest energy ground-state ν(CN) band]—a shift to higher energy of 45 cm^{-1} corresponding to the transiently oxidized Ru(III) center. The second transient band is very intense and covers the region from 1950 to 2100 cm^{-1}; it overlaps heavily with the bleach of the ground-state ν(CN) band which cuts into it generating a double-peaked appearance which is misleading. This overlap means that estimating the position of this intense ν(CN) transient band in these experiments is difficult, but the shift to lower energy is unlikely to be more than ca. 20 cm^{-1}. This transient band corresponds to the spectating Ru(II) center, for which the ν(CN) band is expected to be shifted to lower energy because the bridging ligand has become electron-rich in the MLCT excited state, which will in turn make the Ru(II) center more electron-rich and increase the Ru[d(π)] → CN(π^*) back-bonding. In addition, the electron-richness of the Ru(II) center will augment the $C^{\delta-}-N^{\delta+}$ dipole compared to the ground state, which accounts for the high intensity of this transient band.

The smaller shift to lower energy of this transient compared to the bipyrimidine-bridged complex $[\{Ru(CN)_4\}_2(\mu\text{-bpym})]^{4-}$ (shift of ca. 40 cm^{-1}) is consistent with the larger size of the conjugated π-system in the HAT ligand compared to bpym, which allows the excited electron to delocalize over a greater spatial region such that the spectating Ru(II) center is less affected by the electron density on the bridging ligand. It is also noteworthy that the excited-state lifetime of $[\mathbf{2}]^{4-}$ under these conditions (56 ns) is remarkably longer than that of $[\{Ru(CN)_4\}_2(\mu\text{-bpym})]^{4-}$ (1.2 ns). Others have noted that delocalization of the ligand-based electron in MLCT excited states of metal−polypyridyl complexes results in substantial increases in excited-state lifetimes, and a similar effect appears to be operating here.[26] The greater rigidity of HAT compared to bpym (which can twist about its central C−C bond) may also have a role in inhibiting some deactivation pathways associated with molecular vibrations. As with $[\{Ru(CN)_4\}_2(\mu\text{-bpym})]^{4-}$, the MLCT excited state of $[\mathbf{2}]^{4-}$ is clearly localized on the IR time scale and can be described as $[(NC)_4Ru^{II}(HAT^{\bullet-})Ru^{III}(CN)_4]^{4-}$ with separate transient IR signals for spectroscopically distinct Ru(II) and Ru(III) centers.[27]

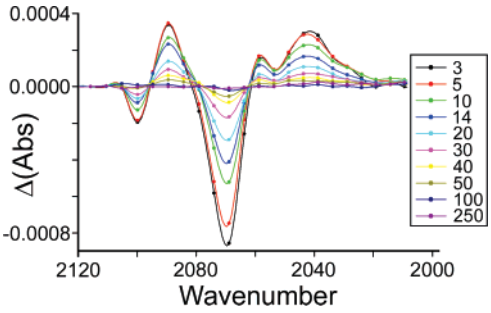

Figure 7. Time-resolved IR difference spectra of $[\mathbf{3}]^{6-}$ in D_2O each measured at several time intervals after excitation. The key shows the time delay after excitation (in nanoseconds) at which each spectrum was recorded.

The TRIR difference spectra of the trinuclear complex Na_6-[**3**] in D_2O at different time delays are shown in Figure 7. The behavior of $[\mathbf{3}]^{6-}$ is generally similar to that of $[\mathbf{2}]^{4-}$ although there are some significant differences. The excited-state spectrum shows a strong bleach of the ground-state ν(CN) band at 2070 cm^{-1} and weaker bleaches at 2055 and 2100 cm^{-1}, which correspond to two weaker ground-state ν(CN) bands. The two lower energy bleaches are superimposed on a broad, intense transient band which covers the region from 2000 to 2100 cm^{-1}. The bleach and transient bands decay synchronously with a time constant of 18 ns. The overlap of ground-state bleach and excited-state transient bands means that in these experiments the maximum of the transient band cannot be accurately determined, but from Figure 7 it appears that that it will be shifted to slightly lower energy than the ground-state bleach, in agreement with what we observed for $[\mathbf{2}]^{4-}$. Thus, this intense transient band can be ascribed to the main ν(CN) band of the spectating Ru(II) centers which are not involved in formation of the MLCT excited state but which are rendered more electron-rich because of the excited-state electron localized on the HAT ligand. The weak higher energy transient band associated with the transiently oxidized Ru(III) center, which is expected at ca. 2110 cm^{-1}, is not apparent. This can be understood with reference to the ground-state FTIR spectrum of $[\mathbf{3}]^{6-}$, which shows that the highest energy ν(CN) band, at 2100 cm^{-1}, is quite intense in this complex. This results in a strong bleach signal in the TRIR at 2100 cm^{-1} which will mask the expected weak transient band in this region. However, it is clear that the MLCT excited state of this complex can also be described as valence-localized on the IR time scale, i.e., $[\{(NC)_4Ru^{II}\}_2(HAT^{\bullet-})$-

(26) Harriman, A.; Ziessel, R. *Chem. Commun.* **1996**, 1707.
(27) (a) Plummer, E. I.; Zink, J. I. *Inorg. Chem.* **2006**, *45*, 6556. (b) Lockard, J. V.; Zink, J. I.; Konradsson, A. E.; Weaver, M. N.; Nelsen, S. F. *J. Am. Chem. Soc.* **2003**, *125*, 13471.

$Ru^{III}(CN)_4]^{6-}$; a delocalized system with all three metal centers equivalent and having an average oxidation state of 2.33+ would not give a low-energy shifted transient band consistent with spectating Ru(II) centers. The lower lifetime of 18 ns for the MLCT excited state of $[\mathbf{3}]^{6-}$ compared to $[\mathbf{1}]^{2-}$ and $[\mathbf{2}]^{4-}$ is consistent with the lower excited-state energy (the "energy-gap law"),[28] although this cannot be used to explain simply why $[\mathbf{2}]^{4-}$ has a longer-lived excited state than $[\mathbf{1}]^{2}$.

To conclude this section, these TRIR studies have highlighted two important points. First, although the ^{3}MLCT excited states of these complexes are essentially nonluminescent in aqueous solution at room temperature, they are relatively long-lived (tens of nanoseconds) which implies that they could be effective energy donors in supramolecular assemblies—an interesting prospect given their remarkable light-harvesting properties as shown in their absorption spectra. Second, for dinuclear $[\mathbf{2}]^{4-}$ and trinuclear $[\mathbf{3}]^{6-}$, the ^{3}MLCT excited states are localized on the IR time scale with spectroscopically distinct Ru(II) and Ru(III) centers generating two sets of transient bands in the ν(CN) region.

Structures of Coordination Networks with Ln(III) Cations. We prepared and structurally characterized coordination networks using the three cyanoruthenate anions with various Ln(III) cations, for two reasons. First, we were interested to evaluate the ability of the complexes to generate structurally novel highly connected networks. The use of Ln(III) cations, which can tolerate higher coordination numbers than d-block ions and therefore are more likely to generate high-dimensionality networks, therefore seemed a sensible choice.[29] Second, many of the Ln(III) ions have low-energy f−f excited states which show luminescence in the near-infrared region, and we were interested to examine the ability of $[\mathbf{1}]^{2-}$, $[\mathbf{2}]^{4-}$, and $[\mathbf{3}]^{6-}$—which absorb light very strongly in the visible region and have reasonable excited-state lifetimes—to act as sensitizers of Ln(III)-based near-IR luminescence following d → f energy transfer, as we have shown in other cyanide-bridged d/f networks.[4a,5a]

Crystalline salts were prepared by slow evaporation of aqueous solutions containing $[\mathbf{1}]^{2-}$, $[\mathbf{2}]^{4-}$, or $[\mathbf{3}]^{6-}$ (as their Na^+ salts) and Ln(III) cations as their chloride or nitrate salts. Ln(III) salts of $[\mathbf{1}]^{2-}$ have two different types of solid-state structure according to the size of the Ln(III) cation. When Ln = Nd, Sm, Eu, and Gd, the crystal structures $[\{Ln(H_2O)_5\}_2\{\mathbf{1}\}_3{\cdot}nH_2O]_\infty$ (Ln = Nd, n = 18; Ln = Sm, n = 11; Ln = Eu, n = 16; Ln = Gd, n = 16) are essentially identical and crystallographically isomorphous; the structure for Ln = Nd is in Figures 8 and 9 (see also Table 3). The structure consists of polymeric two-dimensional sheets in the crystallographic *xy* plane. There are two independent types of $[\mathbf{1}]^{2-}$ unit, containing Ru(1) (with one such unit colored purple in Figure 9) and the other containing Ru(2), which lies on a 2-fold rotation axis; one such example is colored cyan in Figure 9. Each $[\mathbf{1}]^{2-}$ unit based on Ru(1) coordinates one if its four cyanide groups to Nd(1), via N(36), and one of the available bidentate sites on the HAT ligand to another Nd(1), via N(24) and N(14). Each $[\mathbf{1}]^{2-}$ unit based on Ru(2) also interacts with two Nd(1) ions but in both cases via cyanide bridges involving N(64) and its symmetry-equivalent

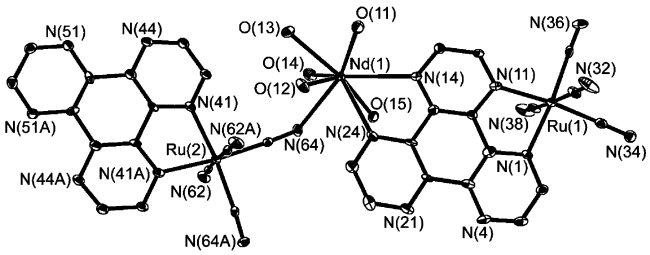

Figure 8. Asymmetric unit of the structure of $[\{Nd(H_2O)_5\}_2\{\mathbf{1}\}_3{\cdot}18H_2O]_\infty$ with additional atoms from adjacent asymmetric units to complete the coordination spheres around the metal centers included.

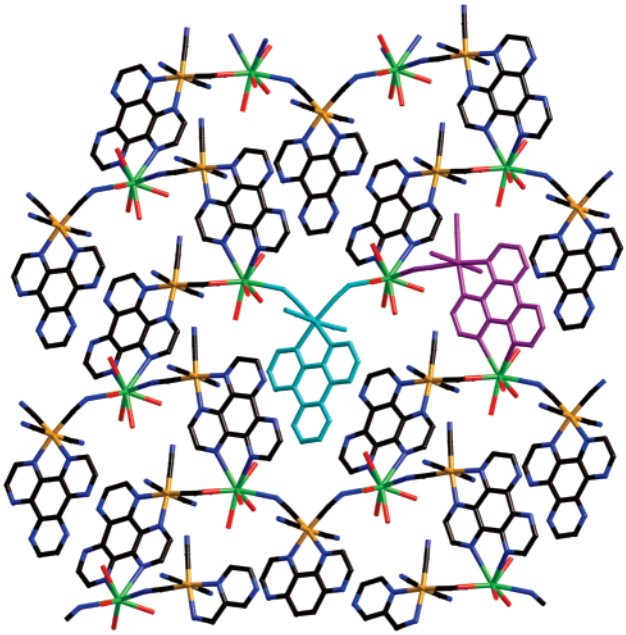

Figure 9. Two-dimensional network structure of $[\{Nd(H_2O)_5\}_2\{\mathbf{1}\}_3{\cdot}18H_2O]_\infty$, with two of the crystallographically independent $[\mathbf{1}]^{2-}$ units colored separately (purple and cyan) for clarity (Nd, green; Ru, orange; O, red; N, blue; C, black).

N(64A). Each Nd(1) center is 9-coordinate, from five water ligands, two cyanide bridges [one to Ru(1) and one to Ru(2)], and a HAT-diimine site from another Ru(1) unit. Since each Nd(III) cation interacts with three $[\mathbf{1}]^{2-}$ dianions and each $[\mathbf{1}]^{2-}$ dianion interacts with two Nd(III) cations, the necessary 3:2 ratio of $[\mathbf{1}]^{2-}$:Nd(III) components results. All of the cyanide ligands that are not involved in coordination to Nd(III) are instead hydrogen-bonded to water molecules as shown by numerous nonbonded N···O separations of <3 Å, involving either water ligands on Nd(III) centers in the layers above/below [e.g., N(32)···O(15), 2.84 Å; N(34)···O(11), 2.88 Å; N(62)···O(12), 2.95 Å] or lattice water molecules [e.g., N(38)···O(2W), 2.84 Å]. Thus, the layers are associated via these interlayer CN···HOH contacts. There are aromatic stacking interactions between partially eclipsed HAT ligands which are parallel to one anotherwith a separation of ca. 3.3 Å between the overlapping fragments.

With the smaller cation Yb(III) a quite different structure $[\{Yb(H_2O)_3(NO_3)_2\}\{Yb(H_2O)_6\}\{\mathbf{1}\}(NO_3)_2(H_2O)_{6.5}]_\infty$ results (Figures 10 and 11; Table 4). The structure is that of two parallel ···Ru−CN−Yb−NC−Ru··· strands oriented along the crystallographic *a*-axis; these two strands are cross-linked by additional Yb(III) centers to give a ladderlike arrangement. The main strands consist of alternating units of $[\mathbf{1}]^{2-}$ and $\{Yb(NO_3)_2$-

(28) Caspar, J. V.; Kober, E. M.; Sullivan, B. P.; Meyer, T. J. *J. Am. Chem. Soc.* **1982**, *104*, 630.
(29) Hill, R. J.; Long, D. L.; Chanpmess, N. R.; Hubberstey, P.; Schröder, M. *Acc. Chem. Res.* **2005**, *38*, 335.

Table 3. Selected Bond Distances in the Structures of $[\{Ln(H_2O)_5\}_2\{\mathbf{1}\}_3 \cdot nH_2O]_\infty$ (Ln = Nd, n = 18; Ln = Sm, n = 11; Ln = Eu, n = 16; Ln = Gd, n = 16)

param	Ln = Nd	Ln = Sm[a]	Ln = Eu[b]	Ln = Gd[c]
Ln(1)−O(11)	2.469(6)	2.388(8)	2.410(8)	2.409(6)
Ln(1)−O(15)	2.439(6)	2.427(9)	2.427(8)	2.396(6)
Ln(1)−N(36)#1	2.497(8)	2.445(12)	2.455(11)	2.446(8)
Ln(1)−N(64)	2.507(8)	2.468(12)	2.460(10)	2.465(7)
Ln(1)−O(14)	2.490(7)	2.487(8)	2.531(9)	2.438(6)
Ln(1)−O(13)	2.472(6)	2.516(9)	2.432(8)	2.409(6)
Ln(1)−O(12)	2.566(7)	2.534(9)	2.452(9)	2.533(6)
Ln(1)−N(14)	2.745(8)	2.718(10)	2.719(10)	2.712(7)
Ln(1)−N(24)	2.742(8)	2.742(10)	2.720(11)	2.713(7)
Ru(1)−C(33)	1.963(10)	1.966(14)	1.938(12)	1.949(9)
Ru(1)−C(35)	1.995(10)	1.976(16)	1.990(13)	1.984(8)
Ru(1)−C(37)	2.030(11)	2.026(15)	2.052(14)	2.040(9)
Ru(1)−C(31)	2.051(11)	2.031(15)	2.043(16)	2.056(9)
Ru(1)−N(11)	2.099(8)	2.086(9)	2.109(10)	2.104(7)
Ru(1)−N(1)	2.113(7)	2.100(12)	2.114(10)	2.109(7)
Ru(2)−C(63)	1.984(9)	1.970(14)	1.993(11)	1.971(8)
Ru(2)−C(61)	2.046(11)	2.052(14)	2.038(14)	2.050(9)
Ru(2)−N(41)	2.116(8)	2.093(10)	2.106(10)	2.099(7)

[a] Symmetry transformations used to generate equivalent atoms: (#1) $-x + 1/2, y - 1/2, -z + 5/2$. [b] Symmetry transformations used to generate equivalent atoms: (#1) $-x + 3/2, y + 1/2, -z + 3/2$. [c] Symmetry transformations used to generate equivalent atoms: (#1) $-x + 1/2, y - 1/2, -z + 3/2$.

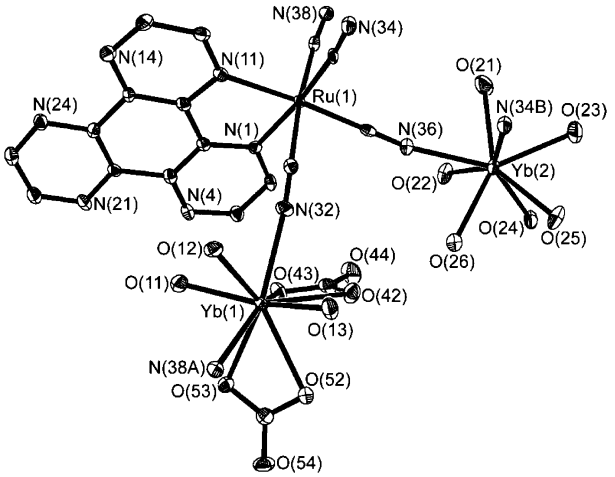

Figure 10. Asymmetric unit of the structure of $[\{Yb(H_2O)_3(NO_3)_2\}\{Yb(H_2O)_6\}\{\mathbf{1}\}(NO_3)_2(H_2O)_{6.5}]_\infty$ with additional atoms from adjacent asymmetric units to complete the coordination spheres around the metal centers included.

$(H_2O)_3\}^+$ in which the trans pair of axial cyanides on each $[\mathbf{1}]^{2-}$ unit coordinate to Yb(III) to generate the one-dimensional chain. The two equatorial cyanides of each $[\mathbf{1}]^{2-}$ unit (in the same plane as the HAT ligand) connect to two $\{Yb(H_2O)_6\}^{3+}$ units which span the two strands, connected to one cyanide from each, forming a $Ru_2Yb_2(\mu\text{-}CN)_4$ square. Thus, each unit of $[\mathbf{1}]^{2-}$ uses all of its cyanide groups to connect to four different Yb(III) centers, two Yb(1) centers in the axial positions which propagate the one-dimensional chains and two Yb(2) centers between the chains which form the cross-pieces of the ladder. The Yb(1) centers are 9-coordinate, from two bidentate nitrates, three water ligands, and two cyanides; the Yb(2) centers are 8-coordinate, from six water ligands and the two cyanides.

The Yb(III) salt of $[\mathbf{2}]^{4-}$ is $[\{Yb(H_2O)_4\}\{Yb(H_2O)_6\}\{Yb(H_2O)_2(NO_3)\}(\mathbf{2})_2 \cdot 20(H_2O)]_\infty$, in which the 8− charge of two $[\mathbf{2}]^{4-}$ units is balanced by three Yb(III) centers and a (coordinated) nitrate ion. The asymmetric unit is shown in Figure 12 (see also Table 5) and reveals the presence of 22-membered

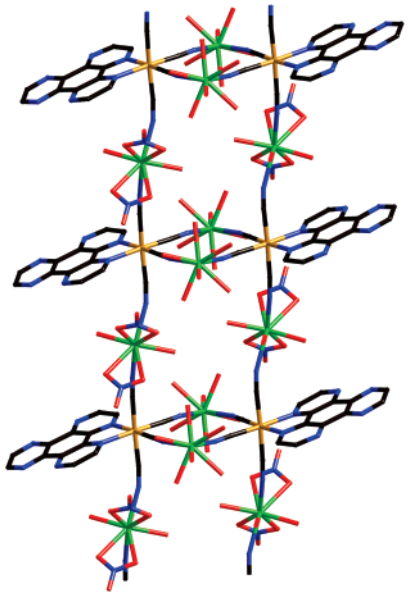

Figure 11. One-dimensional ladder structure of $[\{Yb(H_2O)_3(NO_3)_2\}\{Yb(H_2O)_6\}\{\mathbf{1}\}(NO_3)_2(H_2O)_{6.5}]_\infty$ (Yb, green; Ru, orange; O, red; N, blue; C, black).

Table 4. Selected Bond Distances in the Structure of $[\{Yb(H_2O)_3(NO_3)_2\}\{Yb(H_2O)_6\}\{\mathbf{1}\}(NO_3)_2(H_2O)_{6.5}]_\infty$[a]

Yb(1)−O(11)	2.284(4)	Yb(2)−O(24)	2.327(4)
Yb(1)−O(12)	2.365(4)	Yb(2)−O(25)	2.351(4)
Yb(1)−O(13)	2.273(4)	Yb(2)−O(26)	2.291(4)
Yb(1)−O(42)	2.518(4)	Yb(2)−N(34)#2	2.354(5)
Yb(1)−O(43)	2.397(4)	Yb(2)−N(36)	2.374(5)
Yb(1)−O(52)	2.497(4)	Ru(1)−C(31)	2.025(5)
Yb(1)−O(53)	2.533(4)	Ru(1)−C(33)	1.975(5)
Yb(1)−N(32)	2.367(4)	Ru(1)−C(35)	1.987(6)
Yb(1)−N(38)#1	2.345(5)	Ru(1)−C(37)	2.021(5)
Yb(2)−O(21)	2.305(4)	Ru(1)−N(1)	2.114(4)
Yb(2)−O(22)	2.336(4)	Ru(1)−N(11)	2.111(4)
Yb(2)−O(23)	2.350(4)		

[a] Symmetry transformations used to generate equivalent atoms: (#1) $x + 1, y, z$; (#2) $-x - 1, -y, -z + 1$.

metallamacrocyclic rings containing two $[\mathbf{2}]^{4-}$ units and two Yb(III) ions, i.e., a Ru_4Yb_2 ring with bridging cyanide and HAT ligands. These propagate into a two-dimensional layer structure which is shown in Figure 13 (face-on and edge-on views). Each layer has a complex sandwich-like structure, with the cyanoruthenate units forming the top and bottom of the sandwich and a series of Yb(III) ions in the center of the sandwich. Adjacent parallel layers are associated by hydrogen-bonding interactions involving the numerous lattice water molecules. Of the four independent Ru(II) centers, the number of cyanide ligands acting as bridges to Yb(III) is 3, 2, 3, and 2 for Ru(1)−Ru(4) respectively; i.e. both independent $[\mathbf{2}]^{4-}$ units (examples colored purple and cyan in Figure 13) use five of their eight cyanide ligands to connect to Yb(III) centers. All Yb(III) centers are 8-coordinate: Yb(1) has four bridging cyanides, a bidentate nitrate, and two water ligands. Yb(2) has two cyanides and six water ligands. Yb(3) has four cyanides and four water ligands. Nd(III) and Gd(III) salts of $[\mathbf{2}]^{4-}$ were also prepared but did not give X-ray-quality single crystals and had IR spectra significantly different from that of the Yb(III) complex; on the basis of elemental analyses these are tentatively formulated as $[\mathbf{2}][Nd(NO_3)(H_2O)_5]_2 \cdot 4H_2O$ in which the $[\mathbf{2}]^{4-}$:Ln(III) ratio is 1:2 rather than 2:3 as in the Yb(III) complex.

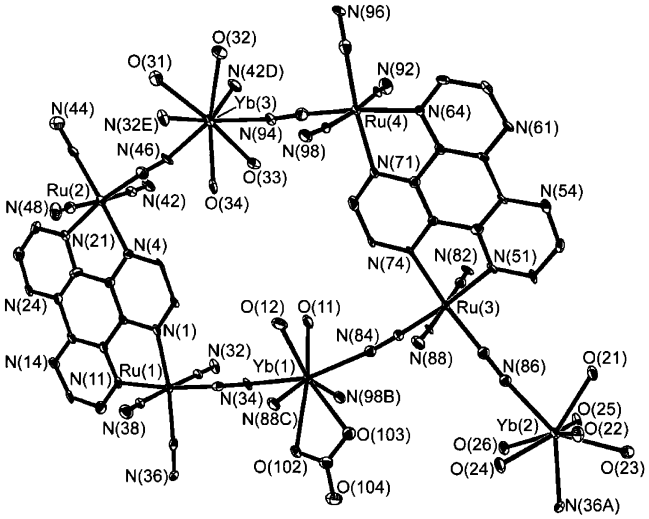

Figure 12. Asymmetric unit of the structure of $[\{Yb(H_2O)_4\}\{Yb(H_2O)_6\}\{Yb(H_2O)_2(NO_3)\}\{\mathbf{2}\}_2{\cdot}20(H_2O)]_\infty$ with additional atoms from adjacent asymmetric units to complete the coordination spheres around the metal centers included.

Table 5. Selected Bond Distances in the Structure of $[\{Yb(H_2O)_4\}\{Yb(H_2O)_6\}\{Yb(H_2O)_2(NO_3)\}\{\mathbf{2}\}_2{\cdot}20H_2O]_\infty$[a]

Yb(1)−O(11)	2.330(7)	Yb(2)−O(21)	2.294(6)
Yb(1)−O(12)	2.330(7)	Yb(2)−O(22)	2.285(7)
Yb(1)−O(102)	2.489(6)	Yb(2)−O(23)	2.364(6)
Yb(1)−O(103)	2.397(6)	Yb(2)−O(24)	2.437(6)
Yb(1)−N(34)	2.311(8)	Yb(2)−O(25)	2.291(7)
Yb(1)−N(84)	2.328(8)	Yb(2)−O(26)	2.304(6)
Yb(1)−N(98)$^{\#1}$	2.345(9)	Yb(2)−N(86)	2.350(8)
Yb(1)−N(88)$^{\#2}$	2.365(9)	Yb(2)−N(36)$^{\#3}$	2.371(8)
Yb(3)−N(46)	2.322(8)	Yb(3)−O(31)	2.387(7)
Yb(3)−N(94)	2.313(8)	Yb(3)−O(32)	2.385(7)
Yb(3)−N(32)$^{\#4}$	2.334(9)	Yb(3)−O(33)	2.389(7)
Yb(3)−N(42)$^{\#5}$	2.364(9)	Yb(3)−O(34)	2.414(7)
Ru(1)−C(31)	2.046(11)	Ru(3)−C(81)	2.041(10)
Ru(1)−C(33)	1.968(10)	Ru(3)−C(83)	1.975(9)
Ru(1)−C(35)	2.017(10)	Ru(3)−C(85)	1.987(10)
Ru(1)−C(37)	2.062(10)	Ru(3)−C(87)	2.031(10)
Ru(1)−N(1)	2.086(8)	Ru(3)−N(51)	2.108(7)
Ru(1)−N(11)	2.116(7)	Ru(3)−N(74)	2.096(8)
Ru(2)−C(41)	2.026(11)	Ru(4)−C(91)	2.083(12)
Ru(2)−C(43)	1.995(10)	Ru(4)−C(93)	1.951(10)
Ru(2)−C(45)	1.998(11)	Ru(4)−C(95)	2.025(11)
Ru(2)−C(47)	2.050(11)	Ru(4)−C(97)	2.052(12)
Ru(2)−N(4)	2.098(8)	Ru(4)−N(64)	2.126(8)
Ru(2)−N(21)	2.104(8)	Ru(4)−N(71)	2.095(8)

[a] Symmetry transformations used to generate equivalent atoms: (#1) $x+1, y, z$; #2, $-x+1, -y+2, -z$; (#3) $-x+2, -y+2, -z$; (#4) $x-1, y, z$; (#5) $-x+1, -y+2, -z+1$.

Crystallization of the trinuclear anion $[\mathbf{3}]^{6-}$ with Nd(III) or Yb(III) affords a three-dimensional polymeric structure based on two-dimensional layers (using the equatorial cyanides in the same plane as the HAT ligand) which are associated by vertical pillars in the form of some of the "axial" cyanide groups. The structure of $[\{\mathbf{3}\}\{Yb(H_2O)_4\}_2{\cdot}13H_2O)_{13}]_\infty$ is shown in Figures 14 and 15 (see also Table 6). The structure consists of two-dimensional sheets in which the six cyanides of each $[\mathbf{3}]^{6-}$ unit that are in the same plane as the HAT ligand all coordinate to Yb(III) centers (Figure 14). Each Yb(III) is 8-coordinate, from four water and four cyanide ligands, with three of the cyanide ligands coming from $[\mathbf{3}]^{6-}$ units within the same layer. These layers are held together by additional bridging cyanide interactions which act as "pillars" between a Ru(II) center in one layer and an Yb(III) center in the adjacent one. Each $[\mathbf{3}]^{6-}$ unit uses

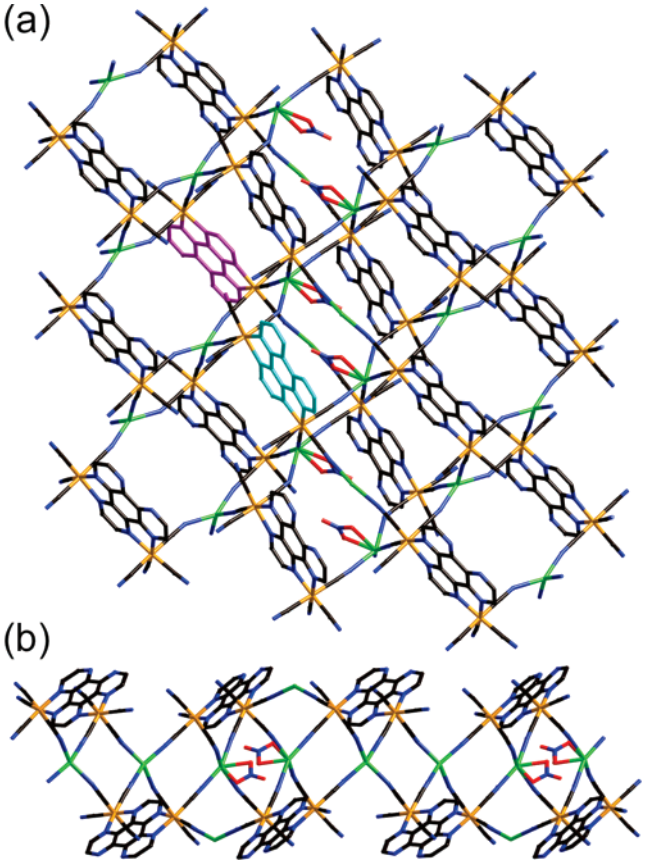

Figure 13. Two views of the two-dimensional network structure of $[\{Yb(H_2O)_4\}\{Yb(H_2O)_6\}\{Yb(H_2O)_2(NO_3)\}\{\mathbf{2}\}_2{\cdot}20H_2O]_\infty$ with two of the crystallographically independent $[\mathbf{2}]^{2-}$ units colored separately (purple and cyan) for clarity (Nd, green; Ru, orange; O, red; N, blue; C, black).

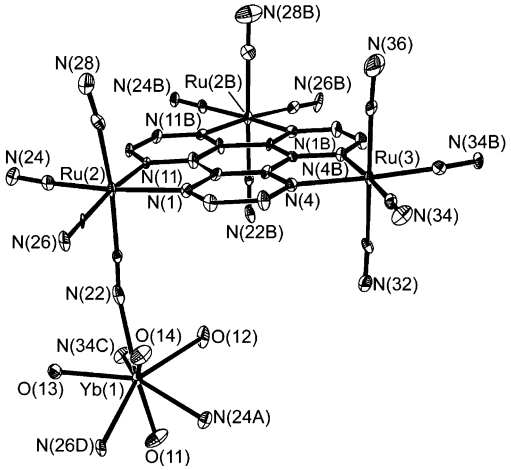

Figure 14. Asymmetric unit of the structure of $[\{\mathbf{3}\}\{Yb(H_2O)_4\}_2{\cdot}13H_2O]_\infty$ with additional atoms from adjacent asymmetric units to complete the coordination spheres around the metal centers included.

two of its six "axial" cyanides in this way, in addition to the six bridging cyanide interactions within each layer. Thus each $[\mathbf{3}]^{6-}$ unit uses 8 of its 12 cyanide ligands in bridging interactions to propagate the network (six in the plane and two axial ones on the same face of the $[\mathbf{3}]^{6-}$ unit connected to the same adjacent layer), with the rest being involved in hydrogen-bonding interactions with some of the lattice water molecules or the Yb-bonded water ligands in adjacent layers. The structure of the Nd(III) analogue $[\{\mathbf{3}\}\{Nd(H_2O)_5\}_2{\cdot}13H_2O)_{13}]_\infty$, which was described in the preliminary Communication,[19] is essentially

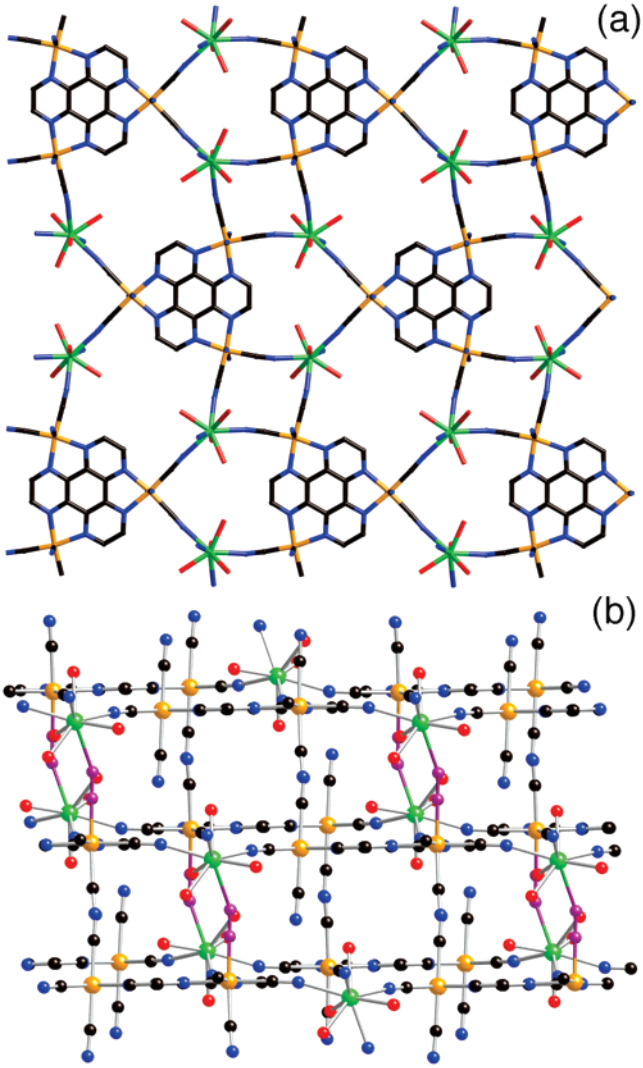

Figure 15. Two mutually perpendicular views of the three-dimensional network structure of $[\{\mathbf{3}\}\{Yb(H_2O)_4\}_2{\cdot}13H_2O]_\infty$, showing (a) the two-dimensional layers and (b) association of these layers via axial bridging cyanides (Yb, green; Ru, orange; O, red; N, blue; C, black). In the bottom view, the axial bridging cyanides are highlighted in purple.

identical with the small difference that the larger Nd(III) ions carry an additional water ligand and are therefore nine-coordinate from four cyanide and five water ligands.

Eight-connecting nodes in metal−organic coordination frameworks are rare, being limited so far principally to Ln(III)-based networks based on 4,4′-bipyridine *N*,*N*′-dioxide (and its relatives) as bridging ligands;[29] 8-fold connectivity is also known in cyanide-bridged networks based on $[W(CN)_8]^{4-}$,[17] which is the maximum connectivity known for a cyanide-based lattice. The eight-connecting behavior of the $[\mathbf{3}]^{6-}$ units described in the above structures is accordingly very unusual but not unprecedented. The possibility to increase this to the maximum possible connectivity of 12, which has only recently been attained in coordination frameworks,[30] is currently under investigation.

Solid-State Photophysical Properties: d → f Energy Transfer. The solid-state coordination networks were subjected to photophysical analysis to (i) evaluate the inherent luminescence characteristics of the chromophores $[\mathbf{1}]^{2-}$, $[\mathbf{2}]^{4-}$, and $[\mathbf{3}]^{6-}$ and (ii) examine the possibility of generating sensitized luminescence from Ln(III) centers with low-energy luminescent f−f states [Nd(III), Yb(III)] by photoinduced d → f energy transfer.[31] The intense charge-transfer absorptions of these cyanoruthenate chromophores in the visible region may make them effective antenna groups to harvest excitation energy which can be passed to the Ln(III) centers, thereby overcoming the inherently low intensities of Laporte-forbidden f−f absorptions and allowing the f−f excited states to be populated indirectly.[4]

As their Na^+ salts $Na_2[\mathbf{1}]$, $Na_4[\mathbf{2}]$, and $Na_6[\mathbf{3}]$, the complexes showed very weak red luminescence in the solid state with corrected emission maxima of ca. 740, 770, and 800 nm, respectively, which became progressively weaker as the number of metal centers increased; for $Na_6[\mathbf{3}]$ the emission was barely detectable, and given the relative insensitivity of our detector in this region, the position of the maximum is subject to a high uncertainty. However, we have shown that the effect of coordinating Lewis-acidic metal cations to the cyanide termini of chromophores of this nature is a substantial increase in ^{3}MLCT energy with a concomitant blue-shift and increase in lifetime of the luminescence,[6] so we examined instead the Gd(III) complexes which, as expected, showed much stronger luminescence. The steady-state luminescence spectra of the Gd(III) adducts of $[\mathbf{1}]^{2-}$, $[\mathbf{2}]^{4-}$, and $[\mathbf{3}]^{6-}$ {hereafter denoted as Gd[**1**], Gd[**2**], and Gd[**3**]) as microcrystalline powders} have (uncorrected) emission maxima at 697, 669, and 681 nm, respectively.[32] We ascribe this to the ^{3}MLCT luminescence characteristic of $[Ru(CN)_4(diimine)]^{2-}$ species,[1−3] which is boosted by the Lewis-acidity of the Gd(III) ions attached to the cyanide termini.[6] This luminescence of course will not be quenched in the Gd(III) adducts because the lowest excited state of Gd(III) is in the UV region, so these emission spectra are

Table 6. Selected Bond Distances in the Structures of $[\{\mathbf{3}\}\{Ln(H_2O)_x\}_2{\cdot}(H_2O)_{13}]_\infty$ (Ln = Nd, x = 5; Ln = Yb, x = 4)

Nd(1)−O(51)	2.482(8)	Yb(1)−O(11)	2.277(8)
Nd(1)−O(52)	2.59(3)	Yb(1)−O(12)	2.320(8)
Nd(1)−O(52′)	2.62(2)	Yb(1)−O(13)	2.319(8)
Nd(1)−O(53)	2.528(7)	Yb(1)−O(14)	2.367(8)
Nd(1)−O(54)	2.496(6)	Yb(1)−N(22)	2.419(11)
Nd(1)−O(55)	2.518(14)	Yb(1)−N(26)$^{\#1\,b}$	2.401(9)
Nd(1)−O(55′)	2.425(17)	Yb(1)−N(34)$^{\#2}$	2.405(9)
Nd(1)−N(44)	2.555(7)	Yb(1)−N(24)$^{\#3}$	2.410(9)
Nd(1)−N(34)$^{\#1\,a}$	2.515(8)	Ru(2)−C(21)	2.007(10)
Nd(1)−N(46)$^{\#2}$	2.525(9)	Ru(2)−C(23)	1.968(11)
Nd(1)−N(48)$^{\#3}$	2.571(9)	Ru(2)−C(25)	1.991(11)
Ru(2)−C(31)	2.032(17)	Ru(2)−C(27)	2.028(12)
Ru(2)−C(33)	1.970(9)	Ru(2)−N(1)	2.123(8)
Ru(2)−C(35)	2.022(15)	Ru(2)−N(11)	2.106(8)
Ru(2)−N(15)	2.104(7)	Ru(3)−C(31)	2.000(15)
Ru(3)−C(41)	2.040(10)	Ru(3)−C(33)	1.992(11)
Ru(3)−C(43)	1.978(9)	Ru(3)−C(35)	1.995(16)
Ru(3)−C(45)	1.975(10)	Ru(3)−N(4)	2.127(8)
Ru(3)−C(47)	1.998(10)		
Ru(3)−N(12)	2.115(7)		
Ru(3)−N(22)	2.111(8)		

[a] Symmetry transformations used to generate equivalent atoms: (#1) $x+1, y, z-1$; (#2) $-x+2, -y+1, -z+1$; (#3) $x+1, y, z$. [b] Symmetry transformations used to generate equivalent atoms: (#1) $-x+4, -y+1, -z+4$; (#2) $x, y, z+1$; (#3) $x+1, y, z$.

(30) (a) Jia, J.; Lin, X.; Wilson, C.; Blake, A.; Champness, N. R.; Hubberstey, P.; Walker, G.; Cussen, E. J.; Schröder, M. *Chem. Commun.* **2007**, 804. (b) Zhang, X.-M.; Fang, R.-Q.; Wu, H.-S. *J. Am. Chem. Soc.* **2005**, *127*, 7670. (c) Li, D.; Wu, T.; Zhou, X.-P.; Zhou, R.; Huang, X.-C. *Angew. Chem., Int. Ed.* **2005**, *44*, 4174.

(31) Ward, M. D. *Coord. Chem. Rev.* **2007**, *251*, 1663.

(32) Applying the correction for the detector response results in these maxima being red shifted by ca. 30 nm. Thus, for Gd[**1**] the corrected emission maximum is at 700 nm, giving a ^{3}MLCT energy of 14 300 cm^{-1}.

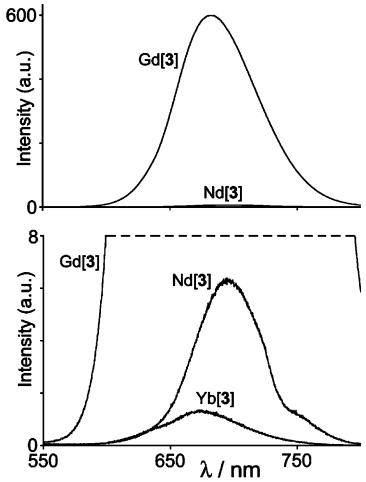

Figure 16. Solid-state luminescence spectra (uncorrected) of Gd[**3**], Nd[**3**], and Yb[**3**] in the visible region showing the residual Ru-based ^{3}MLCT emission, reduced in the case of Nd[**3**] and Yb[**3**] because of Ru → Ln energy transfer.

therefore characteristic of these chromophores coordinated to Ln(III) cations but with no quenching by d → f energy transfer. The spectrum of Gd[**3**] is shown in Figure 16a.

The fact that the highest energy emission in this series comes from Gd[**2**] is, on the face of it, surprising as the ^{1}MLCT absorptions of [**2**]$^{4-}$ are at *longer* wavelength than [**1**]$^{2-}$ in all solvents investigated. This is the usual pattern for dinuclear vs mononuclear complexes based on the same bridging ligand[13] and would suggest that the ^{3}MLCT luminescence of [**2**]$^{4-}$ should be lower in energy than that of [**1**]$^{2-}$ (as we did observe in EtOH/MeOH glasses at 77 K). However, the high sensitivity of the absorption and emission behavior of these cyanoruthenate chromophores to their environment[1−3]—and in particular interactions of the cyanides with additional metal cations[6]—means that the high-energy emission from Gd[**2**] is likely to be a consequence of the environment of the [**2**]$^{4-}$ anion in the crystal. In Gd[**1**], the average number of Ru−CN−Gd bridges is only 1.5/{Ru(CN)$_4$} fragment, whereas in Yb[**2**] this figure is 2.5. Assuming that similar behavior occurs in Gd[**2**], which was not structurally characterized, this greater number of cyanide bridges to Gd(III) ions will result in a greater blue-shift of the ^{3}MLCT emission for [**2**]$^{4-}$ compared to [**1**]$^{2-}$ in the solid state.

Time-resolved measurements were also performed on Gd[**1**], Gd[**2**], and Gd[**3**]. For Gd[**1**] the luminescence decay profile fitted well to a single-exponential decay with τ = 74 ns. The luminescence of Gd[**2**] and Gd[**3**] fitted better to a dual-exponential decay (see Table 7). The presence of multiexponential decay kinetics is a common effect in solid-state samples which contain heterogeneities.[4] Notably, Gd[**2**] has the longest luminescence lifetime of the series (major component, 439 ns). This cannot just be ascribed to the environment of [**2**]$^{2-}$ in the crystal because it is consistent with the pattern observed for ^{3}MLCT lifetimes in D_2O solution obtained from time-resolved IR data; see above.

In the Nd(III) and Yb(III) adducts, the ^{3}MLCT luminescence of the cyanoruthenate donor unit is substantially (but not completely) quenched by energy-transfer to the low-lying f−f levels of these lanthanide(III) cations. This can be seen by (i) a reduction in intensity and lifetime of the Ru(II)-based ^{3}MLCT luminescence {see Figure 16b for the representative series Nd[**3**], Gd[**3**], and Yb[**3**]} and (ii) the appearance of sensitized Ln(III)-based luminescence following the d → f energy transfer. In the Ln[**1**] series (Ln = Nd, Yb) the ^{3}MLCT luminescence (74 ns for Gd[**1**]) is almost completely quenched; there is some residual Ru(II)-based luminescence, meaning that Ru → Ln energy-transfer is not complete, but it is very weak. Sensitized emission from the lanthanide(III) center, in the near-infrared region, could be observed in each case, even when excitation was selectively into the Ru → HAT ^{1}MLCT absorption band at 430 nm [see Figure 17 for an example of sensitized Yb(III)-based emission]. The Ln-based emission lifetimes (Table 7) are characteristically short because of the cross-linked cyanide-bridged network which, as we have observed in other cases, appears to provide an effective mechanism for dispersal of excited-state energy via lattice vibrations.[4a,5a] However it is clear that the strongly absorbing [**1**]$^{2-}$ chromophore can sensitize the Ln(III)-based luminescent excited states, all of which are low enough in energy [Yb(III), $^2F_{5/2}$, 10 200 cm^{-1}; Nd(III), $^4F_{3/2}$, 11 500 cm^{-1}] to act as energy acceptors from the ^{3}MLCT state of [**1**]$^{2-}$ which, on the basis of the solid-state emission from Gd[**1**] is at ca. 14 000 cm^{-1}.[32] On the basis that the Ru → Ln energy transfer requires a gradient of ca. 2000 cm^{-1} at room temperature to prevent thermally activated back energy transfer, the $^4F_{3/2}$ level of Nd(III) at 11 500 cm^{-1} is ideally placed to act as an energy acceptor. For Yb(III) there is only one excited-state which is lower in energy and must be the sole energy acceptor.

A similar general pattern is observed for the Ln[**2**] and Ln[**3**] complexes (Ln = Nd, Yb in both cases); the Ru(II)-based ^{3}MLCT level is strongly quenched compared to Gd[**2**] and Gd[**3**], and sensitized Yb(III)- or Nd(III)-based emission is observed

Table 7. Summary of the Photophysical Properties of the Complexes as Solids (at Room Temperature)[a]

	τ/ns	
complex	Ru → HAT ^{3}MLCT-based[b]	Ln(III)-based
Gd[**1**]	74	
Nd[**1**][c]	<30[e]	48
Yb[**1**][d]	<30[e]	200
Gd[**2**]	439 (major), 97; (400)[f]	
Nd[**2**][c]	150	160
Yb[**2**][d]	<30[e]	295
Gd[**3**]	238, 70 (major); (166)[f]	
Nd[**3**][c]	<30[e]	43 (major), 150
Yb[**3**][d]	too weak to measure	273

[a] Excitation wavelengths: 337 or 430 nm. [b] Ru-based emission lifetime measured at 700 nm. [c] Nd-based emission lifetime measured at 1055 nm. [d] Yb-based emission lifetime measured at 980 nm. [e] Very weak; estimated uncertainty ±10 ns. [f] Fits better to a dual-exponential decay; therefore, two lifetime components are given. The figure in parentheses is the best fit to a single-exponential decay, and this figure is used as a weighted average to estimate energy-transfer rates (see main text).

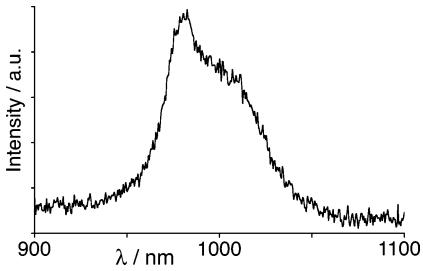

Figure 17. Sensitized Yb(III) luminescence ($^2F_{5/2}$ → $^2F_{7/2}$) from Yb[**2**] on excitation into the Ru-based MLCT absorption manifold at 430 nm.

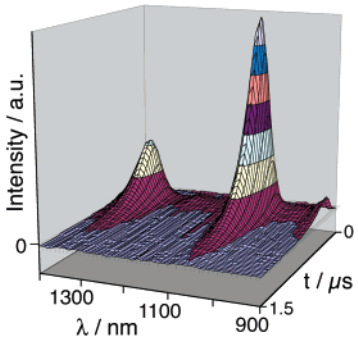

Figure 18. Time-resolved emission profile of Nd[**3**] in the near-IR region showing the Nd(III)-based sensitized emission bands at 1060 nm ($^4F_{3/2} \rightarrow {}^4I_{11/2}$) and 1340 nm ($^4F_{3/2} \rightarrow {}^4I_{13/2}$), using an excitation wavelength of 337 nm.

(Figure 18). The Ln[**2**] series showed some interesting results, with the residual Ru-based emission for Nd[**2**] and Yb[**2**] being stronger and longer-lived than for Nd[**1**] and Yb[**1**] in which the Ru-based emission was almost completely quenched. For the series Gd[**2**], Nd[**2**], and Yb[**2**] the Ru-based luminescence lifetime decreases along the sequence [τ = 400 (weighted average of two components), 150, and 18 ns, respectively], indicating that Yb(III) is a better energy acceptor than Nd(III), with Ru → Ln photoinduced energy-transfer rates k_{EnT} of ca. 4 × 10^6 s^{-1} for Ru → Nd and 5 × 10^7 s^{-1} for Ru → Yb (on the basis of eq 1, where τ_q is the "quenched" lifetime in the presence of Nd or Yb and τ_u is the "unquenched" lifetime in the Gd adduct, taken as 400 ns; see footnote *f* to Table 7).

$$k_{EnT} = 1/\tau_q - 1/\tau_u \qquad (1)$$

Similarly in the series Ln[**3**], Nd[**3**] shows weak residual Ru-based luminescence ($\tau \approx 20$ ns) whereas in Yb[**3**] the Ru-based emission is almost completely quenched (Figure 16b), again implying that Ru → Yb energy transfer is faster than Ru → Nd energy transfer. In this series we can also see nicely how the wavelength of the Ru(II)-based emission (695 nm for Nd[**3**]; 681 nm for Gd[**3**]; 673 nm for Yb[**3**]) is related to the Lewis-acidity of the Ln(III) center,[6] with the smallest and most electropositive ion [Yb(III)] resulting in the most blue-shifted emission from the $[\mathbf{3}]^{6-}$ chromophore. The characteristic Ln(III)-based sensitized emission was evident in every case; Figure 18 shows the time-resolved emission profile from Nd[**3**] following excitation of the $[\mathbf{3}]^{6-}$ chromophore at 337 ns, and the Ln(III)-based lifetimes are collected in Table 7.

Faster energy-transfer to Yb(III) compared to Nd(III) is the reverse of the general pattern that many have observed in d/f systems in which a d-block chromophore has been shown to transfer its excited-state energy much faster to Nd(III) than to Yb(III).[2] This situation arises because many common luminescent d-block fragments [e.g., those based on Re(I), Ru(II), and Pt(II) with polypyridyl-type ligands] have ^{3}MLCT energies in the 16 000−18 000 cm^{-1} range. Nd(III) has a high density of f−f excited states in this region (eight between 11 000 and 18 000 cm^{-1}) which mean that Nd(III) is a very effective energy acceptor from these d-block fragments. However as the ^{3}MLCT energy of the d-block component is reduced, the donor/acceptor spectroscopic overlap with the lower lying excited state of Yb(III) at 10 200 cm^{-1} will increase as the overlap with the higher lying Nd(III) states decreases, and it is accordingly quite reasonable that Yb(III) will be a better energy acceptor than Nd(III) for d-block energy donors with relatively low-energy excited states, as in this case. The relevant Ln(III)-based energy levels are shown in Figure 19.

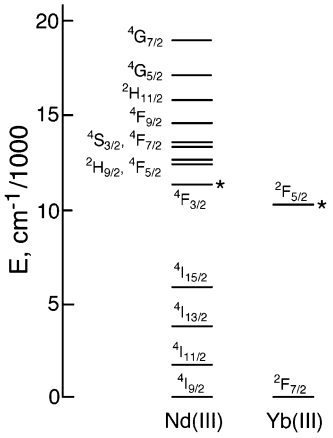

Figure 19. Lower energy levels of Nd(III) and Yb(III). The levels from which luminescence originates are marked with an asterisk.

Conclusions

The series of cyanoruthenate complexes $[\mathbf{1}]^{2-}$, $[\mathbf{2}]^{4-}$, and $[\mathbf{3}]^{6-}$ show an interesting range of spectroscopic and structural properties which exemplify the immense value of this class of complex in both crystal engineering and supramolecular photochemistry. Notable features include (i) the presence of up to 12 cyanide ligands/complex, allowing unusually high connectivity at a single node (the maximum connectivity we observed was eight, in Nd[**3**] and Yb[**3**]), (ii) remarkably strong solvatochromism, which gives these complexes in non-hydrogen-bonding solvents a light-harvesting capacity which substantially exceeds that of many other panchromatic "black" dyes used in solar energy harvesting, (iii) the ability to see valence-localized ^{3}MLCT excited states in $[\mathbf{2}]^{4-}$ and $[\mathbf{3}]^{6-}$ on the basis of time-resolved IR spectra, and (iv) the ability of the chromophores to act as sensitizers for near-infrared luminescence from lanthanide(III) ions in cyanide-bridged coordination networks.

Experimental Section

General Details. The ligand 1,4,5,8,9,12-hexaazatriphenylene (HAT) was prepared as described elsewhere;[33] $K_4[Ru(CN)_6]$ was kindly provided on loan by Johnson Matthey plc. All other reagents, metal salts, and chromatographic materials were purchased from Aldrich, Fluka, or Avocado and used as received.

FT-IR spectra were recorded on a Perkin-Elmer Paragon instrument using an ATR accessory which allowed the spectra of the solids to be determined directly without the need to prepare KBr pellets. UV/vis spectra were recorded on a Cary-50 spectrophotometer. ^{1}H NMR spectra were measured on a Bruker AC-250 spectrometer. Most of the instrumentation used for the time-resolved luminescence measurements in the visible and near-IR regions has been described in detail in previous papers;[34] in addition some measurements were made on a Jobin Yvon-Horiba Fluorolog instrument fitted with a JY TBX picosecond photodetection module and a Hamamatsu R55009-73 detector (cooled to −80 °C using a C9940 housing). The steady-state emission spectra

(33) Sarma, M. S. P.; Czarnik, A. W. *Synthesis* **1988**, 72.
(34) (a) Beeby, A.; Faulkner, S. *Chem. Phys. Lett.* **1997**, *266*, 116. (b) Shavaleev, N. M.; Pope, S. J. A.; Bell, Z. R.; Faulkner, S.; Ward, M. D. *Dalton Trans.*, **2003**, 808. (c) Ronson, T. K.; Lazarides, T.; Adams, H.; Pope, S. J. A.; Sykes, D.; Faulkner, S.; Coles, S. J.; Hursthouse, M. B.; Clegg, W.; Harrington, R. W.; Ward, M. D. *Chem.—Eur. J.* **2006**, *12*, 9299.

at 77 K shown in Figure 5 were measured on a Perkin-Elmer LS-50B luminescence spectrometer

Syntheses. Na^+ Salts of $[1]^{2-}$, $[2]^{4-}$, and $[3]^{6-}$. A solution of HAT (0.12 g, 0.5 mmol) and $K_4[Ru(CN)_6].3H_2O$ (0.84 g, 1.8 mmol) in aqueous HCl at pH 1.3 was heated at reflux with stirring for 48 h and then cooled to room temperature. The resulting dark violet solution was filtered over Celite to remove unreacted HAT and then evaporated to dryness. The solid residue was dissolved in the minimum quantity of water, and MeOH was added to precipitate unreacted $K_4[Ru(CN)_6]\cdot 3H_2O$, which was filtered off. The product was purified by column chromatography on SEPHADEX QAE-25, eluting with aqueous NaI. Use of 0.1 M NaI resulted in elution of orange-red $Na_2[Ru(\mu_2\text{-HAT})(CN)_4]$, Na_2[**1**]; increasing the concentration to 0.2 M then resulted in elution of deep red $Na_4[\{Ru(CN)_4\}_2(\mu_2\text{-HAT})]$, Na_4[**2**], which is the major product; finally use of 0.3 M NaI resulted in elution of violet $Na_6[\{Ru(CN)_4\}_3(\mu_3\text{-HAT})]$, Na_6[**3**]. Solutions of the three complexes so obtained were reduced in volume to 5 cm^3. The products were precipitated by addition of acetone, further recrystallized from H_2O/acetone, and dried in vacuo to give the pure products as a orange-red (mononuclear), deep red (dinuclear), and violet (trinuclear) products. Yields: Na_2[**1**], 25%; Na_4[**2**], 39%; Na_6[**3**], 18%. Conversion to the organic-soluble PPN^+ salts was accomplished using the method in ref 20.

Negative ion ESMS data in H_2O: for Na_2[**1**], *m*/*z* 463 $\{Na[\mathbf{1}]\}^-$, 441 $\{H[\mathbf{1}]\}^-$; for Na_4[**2**], *m*/*z* 346 $\{Na_2[\mathbf{2}]\}^{2-}$, 321 $\{H_2[\mathbf{2}]\}^{2-}$ (both very weak). Na_6[**3**] did not give a signal in ESMS.

^{1}H NMR data (250 MHz, D_2O): for Na_2[**1**], δ 9.19 (2H, s), 9.25 (2H, d, J = 2.7), 9.74 (2H, d, J = 2.7 Hz); for Na_4[**2**], δ 9.33 (2H, d, J = 2.7), 9.64 (2H, s), 9.76 (2H, d, J = 2.7 Hz); for Na_6[**3**], δ 9.66 (6H, s).

$[\{Ru(HAT)\}(\mu\text{-}CN)_4]^{2-}/Ln^{3+}$ Complexes, Ln[1]. A red solution of $Na_2[Ru(HAT)(CN)_4]\cdot 4H_2O$ (0.02 g, 35 μmol) in H_2O (1 cm^3) and the appropriate $Ln(NO_3)_3\cdot 6H_2O$ (0.2 mmol) in water (1 cm^3) was stirred for 10 min. Slow evaporation of the resulting solution over a period of 2−3 weeks resulted in a crop of red crystals in yields of up to 70%; these were filtered off and washed with methanol and dried under vacuum.

$[\{Ru(CN)_4\}_2(\mu_2\text{-HAT})]^{4-}/Ln^{3+}$ Complexes, Ln[2]. A deep red solution of $Na_4[\{Ru(CN)_4\}_2(\mu_2\text{-HAT})]\cdot 8H_2O$ (0.02 g, 23 μmol) in H_2O (1 cm^3) and the appropriate $Ln(NO_3)_3\cdot 6H_2O$ (0.25 mmol) in water (1 cm^3) was stirred for 10 min. Slow evaporation of the resulting solution over a period of 2−3 weeks resulted in a crop of dark red crystals in yields of up to 70%; these were filtered off and washed with methanol and dried under vacuum.

$[\{Ru(CN)_4\}_3(\mu_3\text{-HAT})]^{6-}/Ln^{3+}$ Complexes, Ln[3]. A deep violet solution of $Na_6[\{Ru(CN)_4\}_3(\mu_3\text{-HAT})]\cdot 12H_2O$ (0.015 g, 12 μmol) in H_2O (1 cm^3) and the appropriate $Ln(NO_3)_3\cdot 6H_2O$ (0.25 mmol) in water (1 cm^3) was stirred for 10 min. Slow evaporation of the resulting solutions over a period of 2−3 weeks resulted in a crop of dark blue crystals in yields of up to 60%; these were filtered off and washed with methanol and dried under vacuum.

Analytical and IR spectroscopic data for all new complexes are collected in Table S3 (Supporting Information).

X-ray Crystallography. Suitable crystals were mounted on a Bruker APEX-2 diffractometer equipped with graphite-monochromatized Mo Kα radiation. Details of the crystal, data collection, and refinement parameters are collected in the Supporting Information, and selected structural parameters are collected in Tables 1 and 3−6. After integration of the raw data and merging of equivalent reflections, an empirical absorption correction was applied on the basis of comparison of multiple symmetry-equivalent measurements.[35] The structures were solved by direct methods and refined by full-matrix least-squares on weighted F^2 values for all reflections using the SHELX suite of programs.[36] None of the refinements presented any significant problems. For coordinated and lattice water molecules, H atoms were added only when both of them showed up clearly in a refinement using only low-angle data; they were then fixed in position with O−H distances of 0.85 Å. In all cases there are numerous lattice water molecules which were refined with either 50% or 100% site occupancy as required to generate reasonable thermal displacement parameters.

Time-Resolved Infrared Spectroscopy. TRIR experiments were carried out using the PIRATE apparatus at the Central Laser Facility of the CCLRC Rutherford Appleton Laboratory. This apparatus has been described in detail previously.[37] Ps-TRIR setup: Part of the output from a 1 kHz, 800 nm, 150 fs, 2 mJ Ti-Sapphire oscillator/regenerative amplifier (Spectra Physics Tsunami/Spitfire) was used to pump a white light continuum seeded β-BaB_2O_4 optical parametric amplifier (OPA). The signal and idler produced by this OPA were difference frequency mixed in a type I $AgGaS_2$ crystal to generate tuneable mid-infrared pulses (ca. 150 cm^{-1} fwhm, 1 μJ), which were split to give probe and reference pulses with data points collected every 4−5 cm^{-1}. Second harmonic generation of the residual 800 nm light provided 400 nm pump pulses. Both the pump and probe pulses were focused to a diameter of 200−300 μm in the sample. Changes in infrared absorption at various pump−probe time delays were recorded by normalizing the outputs from a pair of 64-element MCT infrared linear array detectors on a shot-by-shot basis. ns-TRIR spectra were obtained using a Nd:YAG laser (Advanced Optical Technology ACE) as the excitation source and the detection system detailed above.

DFT Calculations. All calculations were performed using the SMP version of the Gaussian 03 program package[38] with the B3LYP functional method.[39] Gaussian was compiled using Intel ifc compiler version 7.1 with ATLAS version 3.6.0[40] and the GOTO implementation of BLAS.[41] In all calculations we used Stuttgart/Dresden pseudo potential on Ru[42] and the D95V basis set on all other atoms.[43] As a result, the calculations for $[\mathbf{3}]^{6-}$ contained 717 basis functions and 225 electrons. No symmetry was taken into account in our calculations, to circumvent problems with cavity generation in the PCM part of the calculations.

In all calculations the following procedure was adopted. Starting from the crystal structure for $[\mathbf{3}]^{6-}$, we first generated $[\mathbf{1}]^{2-}$ and $[\mathbf{2}]^{4-}$; all structures were then optimized. In the case of DMF, solvent interactions were treated using the polarizable continuum model (PCM)[44] and the united atom topological model[45] applied to radii optimized at the Hartree−Fock 6-31(d) level of theory. This set of radii was used to retain compatibility with the implementation of PCM in earlier versions of Gaussian. DMF is not a standard solvent in Gaussian 03. Therefore, the following parameters were used: EPS = 36.7; DENSITY = 0.95; RSOLV = 1.8. To model the solvent interactions in case of water, we added one water molecule to the end of each of the CN^- groups and modeled the bulk of the water interaction via PCM. After obtaining the minimum energy structures, we performed a single-

(35) Sheldrick, G. M. *SADABS*: *A program for absorption correction with the Siemens SMART system*; University of Gottingen: Gottingen, Germany, 1996.

(36) *SHELXTL program system version 5.1*; Bruker Analytical X-ray Instruments Inc.: Madison, WI, 1998.

(37) Towrie, M.; Grills, D. C.; Dyer, J.; Weinstein, J. A.; Matousek, P.; Barton, R.; Bailey, P. D.; Subramaniam, N.; Kwok, W. M.; Ma, C.; Phillips, D.; Parker, A. W.; George, M. W. *Appl. Spectrosc.* **2003**, *57*, 367.

(38) Frisch, M. J.; et al. *Gaussian 03*, revision B.05; Gaussian, Inc.: Wallingford, CT, 2004.

(39) Becke, A. D. *J. Chem. Phys.* **1993**, *98*, 5648.

(40) (a) Whaley, R. C.; Petitet, A.; Dongarra, J. J. *Parallel Comput.* **2001**, *27*, 3. (b) Also available as University of Tennessee LAPACK Working Note No. 147, UT-CS-00-448, 2000 (http://www.netlib.org/lapack/lawns/lawn147.ps).

(41) See the following: http://www.cs.utexas.edu/users/flame/goto.

(42) (a) Nicklass, A.; Dolg, M.; Stoll, H.; Preuss, H. *J. Chem. Phys.* **1995**, *102*, 8942. (b) Cao, X. Y.; Dolg, M. *J. Chem. Phys.* **2001**, *115*, 7348 and references therein.

(43) Dunning, T. H., Jr.; Hay, P. J. In *Modern Theoretical Chemistry*; Schaefer, H. F., III, Ed.; Plenum: New York, 1976; Vol. 3, p 1.

(44) (a) Menucci, B.; Tomassi, J. *J. Chem. Phys.* **1997**, *106*, 5151. (b) Cossi, M.; Barone, V.; Menucci, B.; Tomassi, J. *Chem. Phys. Lett.* **1998**, *286*, 253 and references therein.

(45) Barone, V.; Cossi, M.; Tomassi, J. *J. Chem. Phys.* **1997**, *107*, 3210.

point TD−DFT[46] calculation to obtain excitation energies using tight convergence criteria for the SCF step and ultrafine integrals. During the TD−DFT calculation, solvent was treated in the same way as during the geometry optimization. The final coordinates for $[\mathbf{1}]^{2-}$, $[\mathbf{2}]^{4-}$, and $[\mathbf{3}]^{6-}$ and the aquated analogues $[\mathbf{1}]^{2-}\cdot 4H_2O$, $[\mathbf{2}]^{4-}\cdot 8H_2O$, and $[\mathbf{3}]^{6-}\cdot 12H_2O$, are given in the Supporting Information.

Acknowledgment. We thank the Spanish Ministry of Education and Science for a postdoctoral grant (to J.-M.H.), the EPSRC (U.K.) for additional financial support, and Johnson Matthey for the loan of potassium hexacyanoruthenate. We also thank Dr. Mike Towrie and Dr. Kate Ronayne for experimental assistance with the time-resolved IR spectra measured at the CCLRC Rutherford Appleton Laboratory.

(46) (a) Strattmann, R. E.; Scuseria, G. E.; Frisch, M. J. *J. Phys. Chem.* **1998**, *108*, 4439. (b) Bauernschmidt, R.; Ahlrichs, R. *Chem. Phys. Lett.* **1996**, *256*, 454. (c) Casida, M. E.; Jamorski, C.; Casida, K. C.; Salahub, D. R. *J. Chem. Phys.* **1998**, *108*, 4439.

Supporting Information Available: Complete citation for ref 38, calculated electronic spectral transitions and atomic coordinates for all complexes derived from the GAUSSIAN calculations, routine analytical and IR spectroscopic data for the new complexes, details of the crystal parameters and data collection and refinement details for the crystal structures, and crystallographic CIF files for the new structures. This material is available free of charge via the Internet at http://pubs.acs.org.

JA072672W